# Deep Convective Adjustment of Temperature and Moisture

FIAZ AHMED

*Department of Atmospheric and Oceanic Sciences, University of California, Los Angeles, Los Angeles, California*

ÁNGEL F. ADAMES

*Department of Climate and Space Science and Engineering, University of Michigan, Ann Arbor, Michigan*

J. DAVID NEELIN

*Department of Atmospheric and Oceanic Sciences, University of California, Los Angeles, Los Angeles, California*

(Manuscript received 22 August 2019, in final form 26 March 2020)

ABSTRACT

Simple process models and complex climate models are remarkably sensitive to the time scale of convective adjustment $\tau$, but this parameter remains poorly constrained and understood. This study uses the linear-range slope of a semiempirical relationship between precipitation and a lower-free-tropospheric buoyancy measure $B_L$. The $B_L$ measure is a function of layer-averaged moist enthalpy in the boundary layer (150-hPa-thick layer above surface), and temperature and moisture in the lower free troposphere (boundary layer top to 500 hPa). Sensitivity parameters with units of time quantify the $B_L$ response to its component perturbations. In moist enthalpy units, $B_L$ is more sensitive to temperature than equivalent moisture perturbations. However, column-integrated moist static energy conservation ensures that temperature and moisture are equally altered during the adjustment process. Multiple adjusted states with different temperature–moisture combinations exist; the $B_L$ sensitivity parameters govern the relationship between adjusted states, and also combine to yield a time scale of convective adjustment ~2 h. This value is comparable to $\tau$ values used in cumulus parameterization closures. Disparities in previously reported values of $\tau$ are attributed to the neglect of the temperature contribution to precipitation, and to averaging operations that include data from both precipitating and nonprecipitating regimes. A stochastic model of tropical convection demonstrates how either averaging operations or neglected environmental influences on precipitation can yield $\tau$ estimates longer than the true $\tau$ value built into the model. The analysis here culminates in construction of a precipitation closure with both moisture and temperature adjustment ($q$–$T$ closure), suitable for use in both linearized and nonlinear, intermediate-complexity models.

## 1. Introduction

Interactions between moist convection and its environment shape tropical climate, but remain challenging to understand and parameterize. The adjustment-based convective scheme (Manabe and Strickler 1964; Manabe et al. 1965) represents an early attempt to tackle this issue. In this scheme, parameterized moist convection adjusts the gridscale environment by instantaneously consuming super moist adiabatic lapse rates and supersaturation water vapor content. Betts (1986) and Betts and Miller (1986) modified this scheme, replacing instantaneous adjustment with delayed or "soft" adjustment, and replacing strict moist adiabatic and saturation profiles with empirical reference profiles. In Betts–Miller (BM) type schemes, a single time scale, $\tau$ governs the rate at which gridscale temperature and moisture profiles are relaxed to target profiles, and the adjustment process conveniently subsumes the intricacies of subgrid-scale dynamics.

Mass-flux-based convective schemes (Arakawa and Schubert 1974) surpass the simple BM-type schemes in complexity, but retain a key role for convective adjustment. Specifically, the closures in mass-flux-based schemes are adjustment based, resting upon the convective quasi-equilibrium (QE) hypothesis: convection, as an ensemble, consumes available potential energy (APE): a measure of vertically integrated buoyancy. In strict QE, the rate of consumption is assumed to occur far quicker than the rate at which APE is replenished, yielding near-zero

*Corresponding author*: Fiaz Ahmed, fiaz@ucla.edu

DOI: 10.1175/JAS-D-19-0227.1

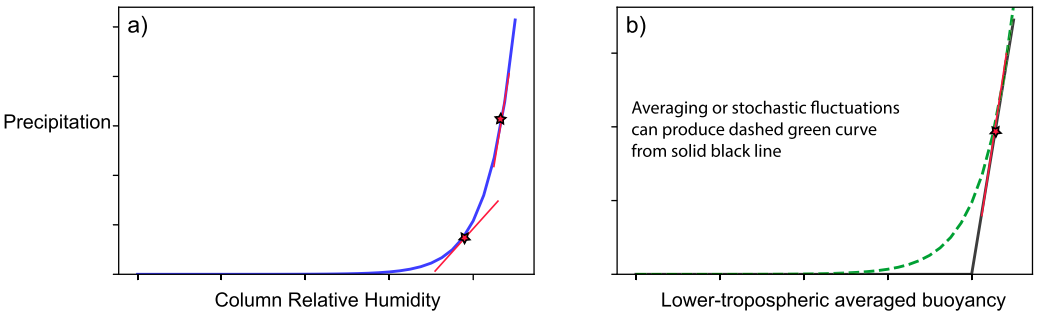


FIG. 1. A schematic explaining the general procedure used to estimate $\tau$ from the observed (a) precipitation–moisture relationship (Bretherton et al. 2004) and (b) precipitation–buoyancy relationship (AN18). The local slope of the curve in each case yields an estimate for $\tau$. In (a), the strong curvature offers infinite base points (stars) around which to estimate the local slope (red lines), leading to unconstrained $\tau$ values. In (b), the strongly linear precipitating regime (black) is characterized by a single value (the slope), which constrains the estimated $\tau$ value. In (b), the nonlinear dashed green curve can emerge from the linear black line in two ways: averaging and from stochastic fluctuations.

APE storage. A finite APE consumption time scale allows for fluctuations about the QE state. The time scale of APE or buoyancy removal is generally taken to be between 1 and 2 h in climate models (e.g., Moorthi and Suarez 1992; Hack 1994; Zhang and McFarlane 1995; Kain 2004; Bechtold et al. 2008), though instances of longer APE removal times do exist [e.g., 8 h in the atmosphere model version 4.0 (AM4.0) double-plume scheme; Zhao et al. 2018]. The APE measure that convection consumes varies across parameterization schemes; convective available potential energy (CAPE) or the cloud work function (Arakawa and Schubert 1974) are popular choices. The precipitation field in both weather and climate models is highly sensitive to the time scale of APE removal (Done et al. 2006; Bullock et al. 2015; Bernstein and Neelin 2016; Qian et al. 2018). The APE removal time scale in mass-flux-based schemes is expected to be related to the adjustment time scale in BM-type schemes. However, a quantitative relationship between the two sets of time scales has not been established.

BM-type convection schemes are widely employed across the modeling hierarchy to understand the two-way interaction between tropical dynamics and moist convection in both intermediate-complexity models (Neelin and Zeng 2000; Frierson 2007a) and toy models (Neelin and Yu 1994; Yu and Neelin 1994; Fuchs and Raymond 2005; Khouider and Majda 2006; Fuchs and Raymond 2007, 2017; Boos and Storelvmo 2016; Stechmann and Hottovy 2017; Ahmed and Neelin 2019). The BM scheme is often modified to only allow moisture adjustment (Sobel et al. 2001; Sobel and Maloney 2012, 2013; Sukhatme 2014; Adames and Kim 2016; Adames and Ming 2018; Adames et al. 2019) when gravity waves are assumed to adjust temperature infinitely fast (Sobel and Bretherton 2000; Sobel et al. 2001).

The solutions in aforementioned models are quite sensitive to the prescribed $\tau$ values. For example, Frierson (2007b) notes that the intraseasonal variability of convectively coupled Kelvin waves (Wheeler and Kiladis 1999; Kiladis et al. 2009) increases with shorter $\tau$ values and vice versa. Similarly, Adames et al. (2019) note that in a simple linearized model with moisture-only adjustment, a $\tau$ value of 2 versus 12 h effectively decided if their resulting dispersion relationship describes a convectively coupled Kelvin wave or a moisture mode, which is thought to describe the Madden–Julian oscillation (Madden and Julian 1971; Zhang 2005; Adames and Wallace 2014). Despite the sensitivity of model solutions to this parameter, the range of $\tau$ values used across models vary from a few hours to tens of hours, to even a few days.

Unclear physical origins contribute to the difficulties in constraining $\tau$ values. Cohen and Craig (2004) link the convective adjustment time scale to the intercloud gravity wave transit time. Betts (1986) links it to the intensity of gridscale vertical velocities, and consequently suggests an upper bound of $\tau = 2$ h to prevent gridscale saturation. Both these studies suggest an implicit spatial-scale dependence for $\tau$; yet, in practice, $\tau$ values are assumed invariant with spatial scale.

Empirical estimates for $\tau$ do exist and rely on the well-known statistical relationship between precipitation and column moisture content (Bretherton et al. 2004; Peters and Neelin 2006; Ahmed and Schumacher 2015; Rushley et al. 2018). Figure 1 depicts the general procedure used to estimate an adjustment time scale from this relationship. The local slope of the curve relating precipitation (usually in units of mm $h^{-1}$) and column moisture content (expressible in units of mm) yields a time scale, which is interpreted as a *moisture adjustment time scale*.

Using this method, Bretherton et al. (2004) estimate $\tau = 12$ h with the observed relationship between daily precipitation and saturation fraction, and $\tau = 16$ h using monthly averaged data. The former estimate was later revised by Rushley et al. (2018) to lie closer to 18 h. Sobel and Bretherton (2003) estimate $\tau = 2.5$ days using composited data from cloud-resolving simulations. These empirical estimates are notably longer than the Betts and Miller (1986) estimate of $\tau = 2$ h with sensitivity experiments in a single-column model. One reason for this discrepancy stems from the lack of a well-defined base point (Fig. 1a) from which to estimate the local slope (Adames 2017), as well as differences in the spatial and temporal scales of the datasets used to generate the precipitation–moisture relationship. The variable local slopes in the precipitation–moisture relationship can be incorporated within nonlinear precipitation closures, but the resulting solutions imply adjustment processes such as algebraic decay, with *no characteristic time scale* for convective adjustment (Yano et al. 2000; Neelin et al. 2009). This study will examine ways in which variable local slopes can emerge in the precipitation–moisture curve—even when a single underlying convective adjustment time scale exists.

Recently, Ahmed and Neelin (2018, hereafter AN18) derived an expression that cast moisture as a buoyancy surrogate, and posited a more general precipitation–buoyancy relationship. Using buoyancy instead of moisture explained the observed land–ocean differences in the precipitation–moisture relationship (Ahmed and Schumacher 2017; Schiro and Neelin 2019). The AN18 precipitation–buoyancy relationship exhibits a large linear range in contrast to the evident nonlinearity in the precipitation–moisture relationship. This linear regime allows for a single robust estimate of the adjustment time scale (Fig. 1b). The linear regime can, however, be distorted by the use of spatiotemporally averaged data or equivalently, by effects of unaccounted influences on precipitation. Estimates of $\tau$ that rely on the slopes of empirical relationships shown in Fig. 1 therefore contain an implicit dependence on the temporal and spatial scale of the underlying dataset that must be elaborated.

In this study we exploit the AN18 precipitation–buoyancy relationship for a set of applications that previously employed the precipitation–moisture relationship: empirically constraining $\tau$ and devising an adjustment-based precipitation closure appropriate for intermediate-complexity models. Additionally, we also aim to explain discrepancies in previous estimates of $\tau$, and relate the moisture and temperature adjustment time scales in BM-type schemes to the analogous time scale for APE removal in mass-flux-based cumulus parameterization closures. In sections 2 and 3, we inspect the implications of the empirical precipitation–buoyancy relationship for convective adjustment time scales. We estimate the sensitivity of buoyancy to thermodynamic variables characterizing the lower free troposphere and boundary layer. In section 4, we construct an empirically informed precipitation closure, with both temperature and moisture components, suitable for use in simple models. In section 5, we use this closure to construct a combined convective adjustment time $\tau_c$, and further show that $\tau_c$ can also be interpreted as the buoyancy or APE removal time scale. In section 6, we posit reasons for discrepancies in prior estimates of $\tau$ associated with the use of spatiotemporally averaged data or with the neglect of the temperature influence on precipitation. We summarize our results and discuss their implications in section 7.

## 2. A simple buoyancy measure

The AN18 derivation begins by considering a plume rooted in the boundary layer and rising moist adiabatically up to the freezing level. The buoyancy $B$ of this plume at pressure level $p$ was defined as

$$B(p) = g\left[\frac{\theta_e(p) - \tilde{\theta}_e^*(p)}{\tilde{\theta}_e^*(p)}\right], \tag{1}$$

where $g$ is acceleration due to gravity, $\theta_e$ is the plume equivalent potential temperature, and $\tilde{\theta}_e^*(p)$ is the environmental saturation equivalent potential temperature. The definition of buoyancy in (1) relies on an enforced separation between plume and environment, which is slightly different from the definition based on density differences in a continuous fluid (Doswell and Markowski 2004).

Only the properties of the tropospheric air below the freezing level were considered in AN18, since lower-tropospheric thermodynamic variations strongly regulate deep convection (Kuang 2008a; Holloway and Neelin 2009; Tulich and Mapes 2010; Raymond and Flores 2016; Tian and Kuang 2019; Powell 2019). The layer below the freezing level was further divided into three coherent layers—within each of which $\theta_e^*$ was assumed invariant. The layer closest to the surface was intended to represent the boundary layer properties, while the other two free-tropospheric layers were intended to resolve variations in thermodynamic profiles. The plume was assumed to conserve $\theta_e$, except upon mixing with environmental air. The extent of mixing was prescribed through a piecewise linear vertical mass-flux profile, characterized by different slopes in each of the three coherent layers. These slopes quantified the relative contribution of each layer to the plume $\theta_e$ as it

ascended to the freezing level. A physics-informed, data-mining exercise was then used to extract optimal values for the mass-flux slopes using data from TRMM 3B42 precipitation (Huffman et al. 2007) and ERA-Interim (Dee et al. 2011) thermodynamic information. This "reverse engineered" mass-flux profile described environmental air flowing into the plume in a vertically thick layer that extended from the surface to the freezing level. This "deep inflow" profile is a commonly observed feature in strong convective systems (e.g., Ferrier and Houze 1989; Kingsmill and Houze 1999; Mechem et al. 2002; Schiro et al. 2018). See section 4 in AN18 for more information on the reverse-engineering procedure. An expression for the average buoyancy $B_L$ in the two layers above the boundary layer was subsequently derived. When precipitation was conditionally averaged by $B_L$, the resulting curves collapsed across oceanic and continental regions. Despite the use of only three layers to resolve the vertical structure and a number of approximations in the derivation, $B_L$ is still an improved measure over other bulk measures such as column water vapor (CWV) in relating precipitation to its thermodynamic environment. Specifically, $B_L$ can be viewed as a more generalized version of bulk measures such as column saturation fraction (Bretherton et al. 2004) or the ordered pair of CWV and column-averaged temperature $\overline{T}$ (Neelin et al. 2009; Kuo et al. 2018).

While any quasi-conserved plume property [e.g., moist static energy (MSE)] can be used to construct $B_L$, $\theta_e$ was used in the AN18 derivation because it has optimal properties in terms of both physics (conservation during moist adiabatic transformations) and mathematical tractability (lack of virtual temperature and ice phase transformations); $\theta_e$, however, is still a nonlinear function of the environmental moisture and temperature. Here, we pursue a simpler expression for $B_L$. In this spirit of simplicity, we assume two coherent layers: the boundary layer (a 150-hPa-thick layer above the surface), and a lower-free-tropospheric layer (a layer that extends from above our nominal boundary layer to 500 hPa). We assume that the mass-flux profile—which specifies environmental mass inflow to the plume—has slopes $a$ and $b$ in the boundary layer and the lower free troposphere, respectively. With these assumptions and following the same steps as in AN18, we can derive the following expression for $B_L$ ($\mathrm{m\,s^{-2}}$):

$$B_L = g\left[w_B\frac{(\theta_{eB}-\theta^*_{eL})}{\theta^*_{eL}} - w_L\frac{\theta^+_{eL}}{\theta^*_{eL}}\right], \tag{2}$$

where $\theta_{eB}$ is the boundary layer averaged $\theta_e$; $\theta^*_{eL}$ is the lower-free-tropospheric-averaged $\theta^*_e$; and $\theta^+_{eL} = \theta^*_{eL} - \theta_{eL}$ is a measure of subsaturation, where $\theta_{eL}$ is the lower-free-tropospheric-averaged $\theta_e$. The following definitions follow for the parameters $w_B$ and $w_L$, which are functions of the amount of mass inflow and pressure thickness within each layer:

$$w_B = \frac{a\Delta p_B}{b\Delta p_L}\ln\left(\frac{a\Delta p_B + b\Delta p_L}{a\Delta p_B}\right), \tag{3}$$

$$w_L = 1 - w_B. \tag{4}$$

Here, $\Delta p_B$ and $\Delta p_L$ are the pressure thicknesses in the boundary layer and the lower free troposphere, respectively. The slopes of the mass-flux profile, $a$ and $b$ control the relative influence of the boundary layer and the lower free troposphere on the plume buoyancy at the freezing level. We will further assume that a single slope characterizes the linear mass-flux profile in both the boundary layer and the lower free troposphere, such that $a = b$. The plume $\theta_e$ is only sensitive to the fractional contribution from each layer, which yields the constraint: $w_b + w_L = 1$. In this study, we only consider data over tropical oceans. We accordingly assume fixed values of $\Delta p_B = 150$ hPa and $\Delta p_L = 350$ hPa, which prove adequate in capturing the leading-order vertical structure variations over tropical oceans that influence the precipitation statistics. These fixed layer depths and the condition that $a = b$ yields $w_B = 0.52$ from (3).

In (2), the first term on the right hand side is CAPE-like: it measures the undilute plume buoyancy based only on lower-free-tropospheric temperature stratification and boundary layer properties, and carries a fractional weighting $w_B$. Since $B_L$ is an integral measure that does not distinguish between positive- and negative-signed values, this term could also be termed CIN-like. The second term is a measure of subsaturation. It can be thought of as the reduction of buoyancy by entrainment of subsaturated free-tropospheric air into the plume. Hence, $w_L = 1 - w_B$ is the penalty imposed by the subsaturated air on $B_L$. The plume buoyancy, as defined in (2) is therefore sensitive to the temperature stratification, boundary layer moist entropy and the dryness of the lower free troposphere. The value of $w_B$ (= 0.52) implies that both the CAPE-like and subsaturation effects are nearly equally important to $B_L$.

We now approximate layer-averaged $\theta_e$ variables in the form of moist enthalpy $e$ using

$$\theta_{eB} \approx \frac{e_B}{\Pi_B}, \tag{5}$$

$$\theta_{eL} \approx \frac{e_L}{\Pi_L}, \tag{6}$$

where $e_B$ and $e_L$ are the $e$ values averaged over the boundary layer and the lower-free-tropospheric layer, respectively. The terms $\Pi_B$ and $\Pi_L$ are similarly layer-averaged values of the Exner function, $\Pi(p) = (p/p_0)^{R_d/C_p}$, with a reference pressure $p_0 = 1000$ hPa. The moist enthalpy, $e = T + q$, where $T$ and $q$ are the temperature and specific humidity, respectively, but $q$ is scaled by the latent heat of vaporization divided by the specific heat of dry air at constant pressure $L_v/c_p$ to have the same units as $T$ (K). Moist enthalpy, therefore, has units of K, as opposed to the more traditional units of J kg$^{-1}$. With the approximations in (5) and (6), we rewrite the buoyancy in (2):

$$B_L \approx \frac{g}{e_L^*}\Pi_L\left(\frac{w_B e_B}{\Pi_B} + \frac{w_L e_L - e_L^*}{\Pi_L}\right). \tag{7}$$

Equation (7) is a simpler version of the buoyancy in (2). The expression eschews the nonlinear $\theta_e$, and involves only $e$: a linear combination of $T$ and $q$. Naturally, $e^* = T + q^*$.

We now pause to ask if $B_L$ as defined in (7) is empirically adequate as a predictor to justify further analysis. To answer, 4-times-daily observed precipitation from TRMM 3B42 at a horizontal resolution of 0.25° are matched to simultaneous values of thermodynamic structures from ERA-Interim from years 2010–14. The data from the four major tropical ocean basins—whose bounds are detailed in AN18—are pooled together to improve sampling, but results here are insensitive to the ocean basin being used.

Figure 2 compares the tropical ocean precipitation conditionally averaged by the $\theta_e$-based $B_L$ from AN18 to the simplified version of $B_L$ in (7). Recall that the simplified version of $B_L$ is based on a two-layer construction with a single mass-flux slope ($a = b$) and the use of moist enthalpy, $e$ instead of $\theta_e$. The different-colored markers indicate different values of temperature averaged between 200 and 1000 hPa $\overline{T}$. Neelin et al. (2009) showed that $\overline{T}$ tracks geographical variations in the value of CWV at which the conditionally averaged precipitation shows a sharp increase. Figure 2a shows how the use of a single buoyancy variable captures both the $\overline{T}$ and CWV dependence of tropical oceanic precipitation. Figure 2c shows precipitation conditionally averaged by two-layer, moist enthalpy version used from (7). Figures 2a and 2c indicate that the approximation of buoyancy by the simplified version does not alter the salient features of the precipitation–buoyancy relationship: the sharp increase in precipitation at near-zero $B_L$. The noticeable difference occurs in the range of sampled $B_L$ values (Fig. 2b vs Fig. 2d). The pdf of $\theta_e$-based $B_L$ extends out to more negative values (Fig. 2b) than the moist enthalpy version. This difference in the spread of the pdfs arises from the greater number of degrees of freedom in the $\theta_e$-based buoyancy (three vertical layers) than the moist-enthalpy-based version (two vertical layers). The results in Fig. 2 are similar when we use $\Delta p_B = 100$ hPa (not shown). Figure 2 justifies the use of the simplified version of $B_L$ from (7), at least over the tropical oceans.

## 3. Computing convective sensitivities to $B_L$

Figure 2 suggests that the appropriate function relating conditionally averaged precipitation, $P$ to $B_L$ would be the ramp function:

$$P = \alpha(B_L - B_c)H(B_L - B_c), \tag{8}$$

where $\alpha$ is the slope that relates the change in $P$ to a unit change in $B_L$. Here, $H$ is the Heaviside function [such that $H(x) = 1$ for $x > 0$, and $H(x) = 0$ for $x \leq 0$]. Precipitation is, therefore, nonzero only when $B_L$ exceeds the critical buoyancy value $B_c$. Equation (8) is also consistent with the underlying hypothesis from AN18 that $P$ begins its rapid increase as buoyant plumes survive to reach the freezing level. The empirical relationship in (8) is convenient because it side-steps the details of microphysics and subgrid-scale dynamics, and directly relates precipitation to gridscale thermodynamics.

The values of both $\alpha$ and $B_c$ are computed from observations, as shown in Fig. 3. The blue scatter in Fig. 3 is $P$ versus $B_L$ for all $\overline{T}$ values from Fig. 2c. A straight line is fit to the blue scatter between $P$ values 1 and 4 mm h$^{-1}$, using linear regression. The slope of the line is $\alpha$ and the $x$ intercept is the critical buoyancy value, $B_c$—which is close to zero. The curvature in the "foot" region near $B_c$ signals a departure from the ramp function; small stochastic fluctuations in the value of $B_c$ can produce this curvature (Stechmann and Neelin 2011; Hottovy and Stechmann 2015). In Fig. 3, the mode of the $B_L$ pdf (in gray scatter) indicates that tropical oceans spend substantial time around $B_L$ values close to $B_c$. The sharp $P$–$B_L$ relationship further suggests that tropical precipitation consumes positive excursions in $B_L$ and produces precipitation in the process. The pdf of $B_L$ and the $P$–$B_L$ relationship, together, are consistent with the QE condition—and variations around it—over tropical oceans. Statistically speaking, convection appears to consume $B_L$ sufficiently fast compared to the typical rate of environmental supply to produce the sharp drop in the pdf of $B_L$, when buoyancy values exceed $B_c$. The slope of the $P$–$B_L$ relationship, $\alpha$, measures the rate of this buoyancy consumption. This reasoning parallels previous arguments based on observed water vapor statistics

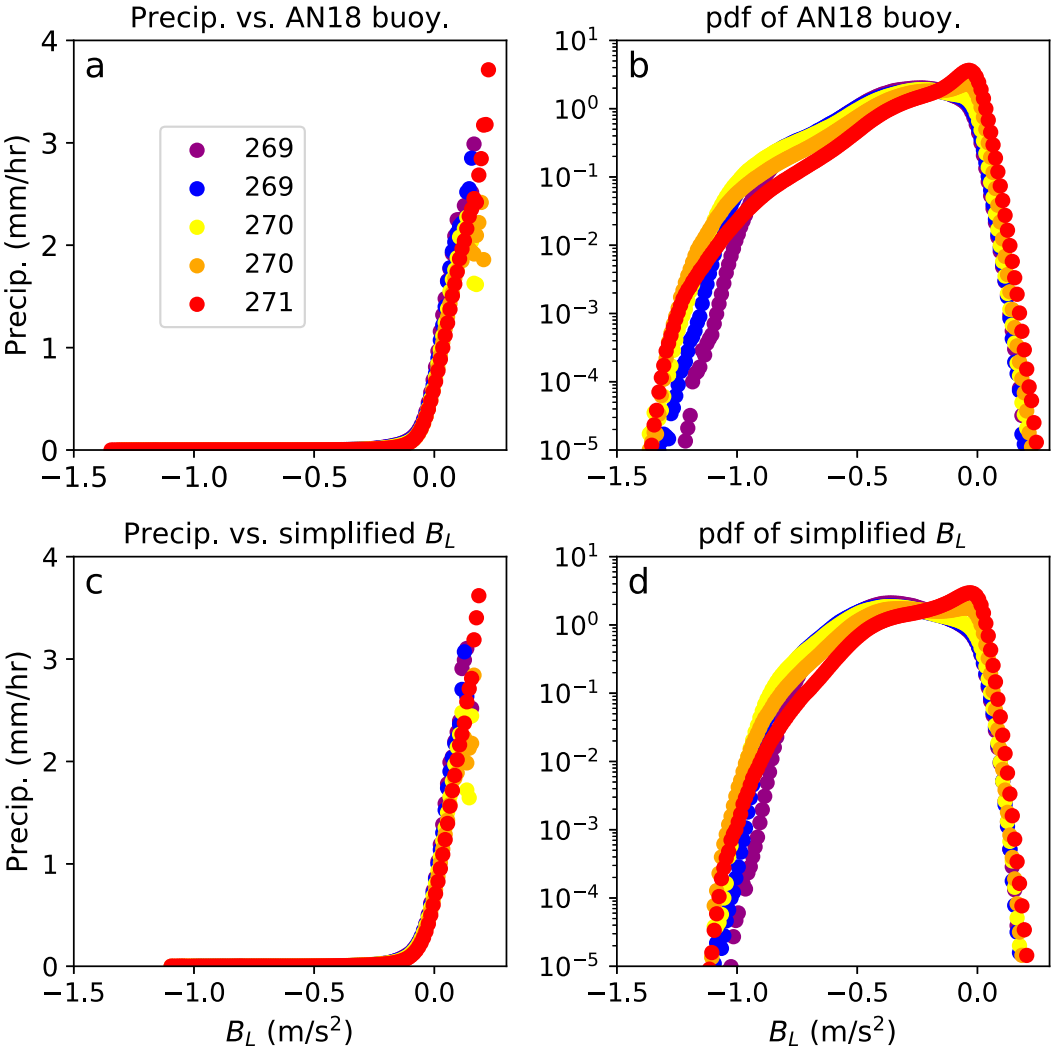


FIG. 2. (a) Tropical oceanic precipitation conditionally averaged by the three-layer $\theta_e$-based buoyancy as in AN18 and (b) the probability density function (pdf) of AN18 buoyancy. (c),(d) As in (a) and (b), but averaged by the two-layer, moist-enthalpy-based buoyancy $B_L$ from (7). The different colors indicated different values of the tropospherically averaged temperature (K).

(e.g., Peters and Neelin 2006; Neelin et al. 2009; Holloway and Neelin 2009) but with an explicit buoyancy formulation. Sections 5b and 5c discuss the consumption of buoyancy by convection in further detail.

### a. *Linearized precipitation–buoyancy relationship*

Consider values of $B_L \geq B_c$. For this set of $B_L$ values, precipitation perturbations, $P'$ arise in response to $B_L$ perturbations, $B'$. The linearized version of (8) is

$$P' = \alpha B' . \tag{9}$$

The expression (7) suggests that $B_L$ is a function of $e_B$, $T_L$ and $q_L$, so we accordingly approximate $B'$ with a Taylor expansion of $B_L$ around a reference value. The approximate linearity of the empirical relation implies insensitivity to the choice of reference above $B_c$ such that:

$$B' = \frac{\partial B_L}{\partial e_B} e'_B + \frac{\partial B_L}{\partial q_L} q'_L + \frac{\partial B_L}{\partial T_L} T'_L + O(e'^2_B, q'^2_L, T'^2_L, \ldots). \tag{10}$$

Using (10) in (9), we get

$$P' = c_p \frac{\Delta p}{g} Q'_c = \alpha \frac{\partial B_L}{\partial e_B} e'_B + \alpha \frac{\partial B_L}{\partial q_L} q'_L + \alpha \frac{\partial B_L}{\partial T_L} T'_L , \tag{11}$$

where precipitation perturbations are related to the integral of the column-averaged latent heating rate $Q_c$, over a column with thickness $\Delta p$. The heat capacity of

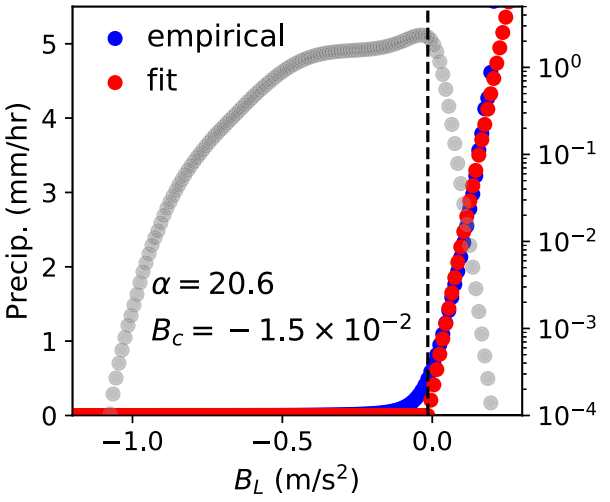


FIG. 3. Precipitation from all tropical oceans conditionally averaged by the moist-enthalpy-based buoyancy (blue) and the accompanying analytic approximation of conditionally averaged precipitation using (8) (red). The values $\alpha$ and $B_c$ are parameters of the approximation. The probability density function of the moist-enthalpy-based buoyancy across all oceans is shown in gray.

dry air is $c_p$. Considering small perturbations allows us to drop terms greater than first order from the Taylor expansion. Now (11) can be rearranged to obtain an expression for $Q_c'$:

$$Q_c' = \frac{e_B'}{\tau_b} + \frac{q_L'}{\tau_q} - \frac{T_L'}{\tau_t}, \tag{12}$$

where $\tau_b$, $\tau_q$, and $\tau_t$ have units of time, and the following definitions:

$$\tau_b = \frac{c_p \Delta p}{\alpha g}\left(\frac{\partial B_L}{\partial e_B}\right)^{-1}, \tag{13}$$

$$\tau_q = \frac{c_p \Delta p}{\alpha g}\left(\frac{\partial B_L}{\partial q_L}\right)^{-1}, \tag{14}$$

$$\tau_t = -\frac{c_p \Delta p}{\alpha g}\left(\frac{\partial B_L}{\partial T_L}\right)^{-1}. \tag{15}$$

From (12), one might be tempted to conclude that the buoyancy adjustment proceeds in three independent pieces with associated adjustment time scales: $\tau_b$, $\tau_q$, and $\tau_t$. We show in section 5b that this interpretation is incorrect, and that a single time scale rules the purely convective response. The column-integrated heating will have to balance the drying; this balance ultimately constrains the rates of consumption, which as we show in section 5 controls the convective adjustment time scale. For now, it is useful to examine the physical insights offered by the time scales $\tau_b$, $\tau_q$, and $\tau_t$. Since these time scales emerge from the partial derivatives of $B_L$, they can be viewed as measures of the sensitivity of convection to perturbations $e_B'$, $q_L'$, and $T_L'$. The partial derivatives in (13)–(15) can be expressed in terms of the base-state variables, using (7):

$$\frac{\partial B_L}{\partial e_B} = \frac{g\Pi_L}{\overline{e}_L^*}\frac{w_B}{\Pi_B}, \tag{16}$$

$$\frac{\partial B_L}{\partial q_L} = \frac{g}{\overline{e}_L^*} w_L, \tag{17}$$

$$\frac{\partial B_L}{\partial T_L} = -\frac{g}{\overline{e}_L^*}\Pi_L\left[\left(\frac{w_B}{\Pi_B}\frac{\overline{e}_B}{\overline{e}_L^*} + \frac{w_L}{\Pi_L}\frac{\overline{e}_L}{\overline{e}_L^*}\right)\left(1 + \frac{L_v \overline{q}_L^*}{R_v \overline{T}_L^2}\right) - \frac{w_L}{\Pi_L}\right], \tag{18}$$

where overbars denote the base state variables. In deriving (16)–(18), we have used the relations: $e_L = q_L + T_L$ and $e_L^* = q_L^* + T_L$. We have also employed the Clausius–Clapeyron relationship:

$$\frac{\partial q_L^*}{\partial T_L} = \frac{L_v \overline{q}_L^*}{R_v \overline{T}_L^2};$$

$L_v$ and $R_v$ are the latent heat of vaporization and the gas constant of water vapor, respectively. The partial derivatives in (16)–(18) exist entirely in the form of base state properties. At this point, we choose our base state as the set of conditions that have $B_L$ slightly greater than $B_c$ ($B_L = 0.015\,\mathrm{m\,s^{-2}}$). This allows us to relate both positive and negative signed $B_L$ perturbations to corresponding precipitation perturbations. Whereas when $B_L = B_c$, only positive perturbations of $B_L$ induce precipitation changes.

Observed base state properties—see Table 1—are plugged into (16)–(18) along with values for $w_B = 0.52$ and $w_L = 0.48$ implied by the assumed layer depths and the linear mass-flux profile. The following estimates for convective sensitivities, in units of hours, are then derived:

$$\tau_t \approx 2.7\,\mathrm{h}, \tag{19}$$

$$\tau_q \approx 11.3\,\mathrm{h}, \tag{20}$$

$$\tau_b \approx 11.5\,\mathrm{h}. \tag{21}$$

The expressions (19)–(21) show two well-separated time scales: one associated with temperature sensitivity, and the other with moisture sensitivity. The strength of the precipitation response for base states with $B_L \geq B_c$ is encapsulated in the single parameter $\alpha$, which characterizes the linear precipitating regime in Fig. 3. Fixing

TABLE 1. Table of parameters used to estimate adjustment times. Parameters $\Pi_B$ through $e_B$ are conditionally averaged for $B_L = 0.015\,\mathrm{m\,s^{-2}}$.

| Quantity | Description | Value |
|---|---|---|
| $\Delta p_B$ | Pressure thickness of the boundary layer | 150 hPa |
| $\Delta p_L$ | Pressure thickness of the lower free troposphere | 350 hPa |
| $w_B$ | Boundary layer contribution to $B_L$ | 0.52 |
| $w_L$ | Lower free troposphere contribution to $B_L$ | 0.48 |
| $\Delta p$ | Pressure thickness of the column | 800 hPa |
| $\alpha$ | Slope of $P$–$B_L$ relationship (Fig. 3) | $20.6\,\mathrm{mm\,h^{-1}\,(m\,s^{-2})^{-1}}$ |
| $B_c$ | Critical buoyancy for precipitation pickup (Fig. 3) | $-1.5\times10^{-2}\,\mathrm{m\,s^{-2}}$ |
| $\Pi_B$ | Boundary layer average of Exner function | 0.97 |
| $\Pi_L$ | Lower-free-tropospheric average of Exner function | 0.88 |
| $q_L^*$ | Lower-free-tropospheric average of saturation moisture | 23.43 K |
| $T_L$ | Lower-free-tropospheric average of temperature | 280.31 K |
| $e_L$ | Lower-free-tropospheric average of moist enthalpy | 300.16 K |
| $e_L^*$ | Lower-free-tropospheric average of saturation moist enthalpy | 300.93 K |
| $e_B$ | Boundary layer average of moist enthalpy | 332.88 K |

$\alpha$ implies insensitivity of the precipitation response to the base state. Indeed, the time scales listed in (19)–(21) remain robust to the choice of base states with $B_L \geq B_c$ (not shown). Capturing the precipitation with a smoother function, [e.g., the exponential in Bretherton et al. (2004) from daily averaged data] offers multiple valid base states for linearization, which consequently yields multiple estimates for the convective adjustment time scale (Adames 2017). A discussion on why the curve resembles an exponential function is presented in section 6.

The derivation of (12) from (9) involves relating column-averaged heating rate to layer-averaged enthalpies. An alternative derivation can relate column-integrated heating to layer-integrated enthalpies. This derivation will reduce the values of $\tau_t$, $\tau_q$, and $\tau_b$, but will preserve the separation between $\tau_t$ and $\tau_q$—which as we will see, is what ultimately controls the convective adjustment time scale. Also note that splitting $e_L$ into its constituent $T_L$ and $q_L$ implies a loss of the conservation properties associated with the balance between heating and drying. It is nevertheless useful to explicitly write out the dependence of $B_L$ on $T_L$ and $q_L$, since most governing equation sets contain separate prognostic equations for temperature and moisture. This split allows (12) and its nonlinear version to be directly employed as a precipitation closure in such equation sets—as demonstrated in sections 4 and 5.

### b. Temperature versus moisture sensitivity

Temperature perturbations ($T_L'$) play a different role in the convective response than either moisture ($q_L'$) or boundary layer enthalpy ($e_B'$) perturbations. For instance, the negative sign in front of $T_L'$ in (12) indicates that precipitation acts to remove lower-free-tropospheric *cold anomalies*. This cold-anomaly response is partly consistent with the idea that convection eliminates positive lapse rate anomalies (Manabe et al. 1965; Betts 1986). We only use a lower-free-tropospheric temperature, so the cold-anomaly response also reflects the CIN-controlled view of convection (Mapes 1997, 2000; Raymond et al. 2003; Raymond and Fuchs 2007), where negative lower-tropospheric temperature anomalies erode a deep CIN layer (Raymond et al. 2003; Kuang 2010; Tulich and Mapes 2010; Fuchs et al. 2014; Herman et al. 2016), and elicit a precipitation response.

To elucidate the physical basis for why $\tau_t$ is noticeably smaller than $\tau_q$, substitute $\overline{e}_B = \overline{\theta}_{eB}\Pi_B$ and $\overline{e}_L = \overline{\theta}_{eL}\Pi_L$ back into (17) and (18), and assume $w_B = w_L$ to obtain

$$\gamma = \frac{\tau_q}{\tau_t} \approx (2 + \gamma_{\mathrm{cape}} - \gamma_{\mathrm{subsat}})\eta_L - 1, \tag{22}$$

where

$$\gamma_{\mathrm{cape}} = \frac{\overline{\theta}_{eB} - \overline{\theta}^*_{eL}}{\overline{\theta}^*_{eL}},$$

$$\gamma_{\mathrm{subsat}} = \frac{\overline{\theta}^+_{eL}}{\overline{\theta}^*_{eL}},$$

$$\eta_L = 1 + \frac{L_v \overline{q}^*_L}{R_v \overline{T}^2_L} = \Pi_L \frac{\partial \theta^*_{eL}}{\partial T_L}.$$

Equation (22) contains three distinct and relevant base-state properties:

1) $\gamma_{\mathrm{cape}}$, a measure of the lower-free-tropospheric plume stability is impacted by differences between the boundary layer $\theta_e$ and the lower-free-tropospheric $\theta^*_e$.
2) $\gamma_{\mathrm{subsat}}$ is the degree of subsaturation in the lower free troposphere. This term represents the effects of plume dilution by the ambient subsaturated air.

3) $\eta_L$ is a factor that handles the linearized translation between $\theta^*_{eL}$ and $T_L$. It includes a term due to the direct effect of temperature, and one due to the Clausius–Clapeyron relationship. The former direct effect tracks changes to the ambient $\theta^*_{eL}$ against which the plume $\theta_e$ is being compared to. The latter effect captures the influence of temperature changes on the ambient saturation levels. For our assumed base state values, $\eta_L \approx 2.5$.

We find that for base states on the verge of conditionally averaged precipitation ($B_L \approx B_c$), $\gamma_{\text{cape}} \approx \gamma_{\text{subsat}}$ (not shown). So (22) reduces to

$$\gamma \approx 4.$$

For typical conditions, the ratio of convective sensitivity to temperature versus moisture perturbations is about a factor of 4, when expressed in common units of moist enthalpy. For the numerical values in (19)–(20), $\gamma = 4.2$. Changes in $T_L$ impact both the stability and subsaturation components of $B_L$—as seen from the factor $\eta_L$ in (22). Changes in $q_L$, on the other hand, only impact $B_L$ by modifying the environmental subsaturation $\theta^+_{eL}$. The $B_L$ measure is agnostic to boundary layer temperature versus moisture perturbations; it responds to the combined boundary layer moist entropy ($\theta_{eB}$) changes by modifying the plume stability. Convection, in this sense, is more sensitive to lower-free-tropospheric temperature anomalies than to lower-free-tropospheric moisture or boundary layer moist enthalpy anomalies. Note also that $\gamma$ is dependent on the base state stability parameters, $\gamma_{\text{cape}}$ and $\gamma_{\text{subsat}}$. In more unstable base states, that is, when $\gamma_{\text{cape}} > \gamma_{\text{subsat}}$, the separation between $\tau_t$ and $\tau_q$ will widen.

It is worth considering the spatial scales for which the time scales derived using (13)–(15) are applicable. The analysis in this section relies on the statistical relationship displayed in Fig. 3, particularly on the slope of the $P$–$B_L$ relationship. The scales of applicability are therefore implied by the grid size of the ERA-Interim and TRMM 3B42 datasets used to produce Fig. 3, which is ~800 km$^2$. Coarse-graining above these spatial scales can distort the linearity and consequently, the slope of the $P$–$B_L$ relationship, as discussed in section 6. However, previous results from the coarse-graining of the precipitation–CWV relationship suggests that this distortion is gradual (see Fig. 8 in Kuo et al. 2018), with similar results for the precipitation pickup holding even for a 1° grid cell, that is, ~$10^4$ km$^2$. We therefore use $10^4$ km$^2$ as a rough upper bound for which the derived time scales in (13)–(15) are valid. For spatial scales finer than our dataset, preliminary examination using the 0.1° ERA5 dataset (Hersbach et al. 2019) suggests that the slope of the $P$–$B_L$ relationship is not greatly modified (not shown). In fact, precipitation appears to be robustly related to column saturation fraction even for grid sizes ~1 km$^2$ in cloud-resolving simulations (Wang and Sobel 2011; Igel et al. 2017; Igel 2017). There is, therefore, a strong suggestion that the $P$–$B_L$ relationship and the time scales in (13)–(15) are robust at spatial scales finer than that of the dataset used in this study. The smallest spatial scales for which the $P$–$B_L$ relationship remains unaltered is worth examination in future work.

## 4. The $q$–$T$ closure

Equations (8) and (12) constitute simple precipitation closures for use in vertically resolved models with separate prognoses of the boundary layer and the free troposphere. Precipitation closures in many models of minimal and intermediate complexity, however, involve column-integrated variables (Neelin and Yu 1994; Yu and Neelin 1994; Neelin and Zeng 2000; Fuchs and Raymond 2002; Sugiyama 2009; Sobel and Maloney 2012; Adames and Kim 2016). We accordingly modify our closures for use in such models, whose thermodynamic budget equations resemble

$$\frac{\partial \hat{q}}{\partial t} = S_q + D_q - P, \tag{23}$$

$$\frac{\partial \hat{T}}{\partial t} = S_T + D_T + \hat{Q}_c, \tag{24}$$

where $\hat{T}$ and moisture $\hat{q}$ are the column-integrated temperature and moisture, respectively. Here, $S_q$ and $S_T$ are source terms excluding precipitation $P$ and column-integrated convective heating $\hat{Q}_c$, respectively. The transport terms for moisture and temperature are $D_q$ and $D_T$, respectively, and $\hat{Q}_c$ is assumed equivalent to $P$. The variables $\hat{T}$ and $\hat{q}$ could represent either full variables or fluctuations around a mean state.

We now assume that the layer-averaged thermodynamic variables are linearly related to their column-integrated counterparts, such that

$$(T_L, q_L, T_b, q_b) = \frac{g}{\Delta p}\left(\frac{\hat{T}}{\Lambda_{\text{TL}}}, \frac{\hat{q}}{\Lambda_{\text{qL}}}, \frac{\hat{T}}{\Lambda_{\text{TB}}}, \frac{\hat{q}}{\Lambda_{\text{qB}}}\right), \tag{25}$$

where $\Delta p$ is the depth of the column, $\Lambda_{\text{TL}}$ is the ratio between the column-integrated temperature $\hat{T}$ and the lower-free-tropospheric-integrated temperature $T_L$, and similarly for $\Lambda_{\text{qL}}$, $\Lambda_{\text{TB}}$, and $\Lambda_{\text{qB}}$. Using (25) and (12), we obtain the following definitions for measures of

convective sensitivity to column-integrated moisture $\tilde{\tau}_q$ and temperature $\tilde{\tau}_t$:

$$\tilde{\tau}_q = \left(\frac{1}{\Lambda_{\mathrm{qB}}\tau_b} + \frac{1}{\Lambda_{\mathrm{qL}}\tau_q}\right)^{-1}, \tag{26}$$

$$\tilde{\tau}_t = \left(\frac{1}{\Lambda_{\mathrm{TL}}\tau_t} - \frac{1}{\Lambda_{\mathrm{TB}}\tau_b}\right)^{-1}. \tag{27}$$

Transforming $\tau_t$, $\tau_q$ and $\tau_b$ to $\tilde{\tau}_t$ and $\tilde{\tau}_q$ inevitably introduces assumptions about the vertical structure of moisture and temperature perturbations. If $A(p)$ and $B(p)$ are the vertical structures of temperature and moisture variations, respectively, then

$$\Lambda_{\mathrm{TL}} = \frac{\hat{A}}{\hat{A}_L}\frac{\Delta p_L}{\Delta p}; \quad \Lambda_{\mathrm{qL}} = \frac{\hat{B}}{\hat{B}_L}\frac{\Delta p_L}{\Delta p};$$

$$\Lambda_{\mathrm{TB}} = \frac{\hat{A}}{\hat{A}_B}\frac{\Delta p_B}{\Delta p}; \quad \Lambda_{\mathrm{qB}} = \frac{\hat{B}}{\hat{B}_B}\frac{\Delta p_B}{\Delta p};$$

where $\hat{A}$ and $\hat{B}$ are mass-weighted, vertical integrals of $A$ and $B$ over the column; $\hat{A}_L$ and $\hat{B}_L$ are integrals over the lower free troposphere; $\hat{A}_B$ and $\hat{B}_B$ are integrals over the boundary layer. Consider two limiting cases for temperature and moisture fluctuations:

1) *Free-tropospheric fluctuations only*: If temperature and moisture fluctuations are absent in the boundary layer ($\tau_b \to \infty$), and if the vertical structure of thermodynamic variations follow the first empirical orthogonal functions (EOFs) of the temperature and moisture time series from Nauru (as in Holloway and Neelin 2009; also see appendix, Fig. A1), then $\Lambda_{\mathrm{TL}} = 1.1$ and $\Lambda_{\mathrm{qL}} = 0.6$, which yields $\tilde{\tau}_t \approx 2.9$ h and $\tilde{\tau}_q \approx 6.7$ h.
2) *Full-tropospheric fluctuations*: When boundary layer variations from the first EOFs of the Nauru time series are included, $\Lambda_{\mathrm{TL}} = 1.0$, $\Lambda_{\mathrm{qL}} = 0.6$, $\Lambda_{\mathrm{TB}} = 1.7$, and $\Lambda_{\mathrm{qB}} = 1.1$, which leads to $\tilde{\tau}_t \approx 3.1$ h and $\tilde{\tau}_q \approx 4.4$ h.

While $\tilde{\tau}_t \sim \tau_t$, $\tilde{\tau}_q$ is substantially smaller than $\tau_q$ for both cases 1) and 2) above. This reduction is largely due to the bottom-heavy vertical structure of moisture variations. The linearized moisture–temperature ($q$–$T$) closure becomes

$$P' = \frac{\hat{q}'}{\tilde{\tau}_q} - \frac{\hat{T}'}{\tilde{\tau}_t}, \tag{28}$$

and its nonlinear version can be written equivalently by expressing (8) as

$$P = \left(\frac{\hat{q}}{\tilde{\tau}_q} - \frac{\hat{T}}{\tilde{\tau}_t} - \alpha B_c\right) H(B_L - B_c), \tag{29}$$

or

$$P = \left[\frac{(\hat{q} - \hat{q}_c)}{\tilde{\tau}_q} - \frac{(\hat{T} - \hat{T}_c)}{\tilde{\tau}_t}\right] H(B_L - B_c). \tag{30}$$

Here, $\hat{q}_c$ and $\hat{T}_c$ are column-integrated moisture and temperature values, respectively, such that

$$B_L(\hat{q}_c, \hat{T}_c) = \alpha^{-1}\left(\frac{\hat{q}_c}{\tilde{\tau}_q} - \frac{\hat{T}_c}{\tilde{\tau}_t}\right) = B_c. \tag{31}$$

Convection is now assumed to act on the large-scale environment by adjusting $\hat{q}$ to $\hat{q}_c$, and $\hat{T}$ to $\hat{T}_c$, respectively. Here, the combination ($q_c$, $T_c$) denotes the set of all $\hat{q}$ and $\hat{T}$ values that mark the QE or adjusted state.

Closures (28) and (30) match the BM scheme modified for use in the quasi-equilibrium tropical circulation model (QTCM; Neelin and Zeng 2000). Note, however, that the BM scheme makes two *separate* postulates about moisture and temperature adjustment. The closures in (28) and (30), in contrast, emerge from a single empirically informed postulate about how precipitation consumes $B_L$. This closure is also similar to the CIN-saturation fraction closures proposed in Fuchs and Raymond (2002) and Raymond and Fuchs (2007). These studies separated their precipitation response into ''moisture adjustment'' and ''buoyancy adjustment'' components—with the latter incorporating the effects of CAPE and CIN. In the closure implied by (28) and (30), moisture and temperature fluctuations are two pieces in a single adjustment process that encapsulates the effects of dilution, static stability, and boundary layer enthalpy variations. However, the mathematical form of the $q$–$T$ closure is equivalent to the CIN-saturation fraction closures. Although the CIN-based assumptions were not explicitly included, they implicitly enter our analysis when considering separate thermodynamic fluctuations in the boundary layer and the lower free troposphere. The closures in (28) and (30) are also consistent with empirical analyses expressing precipitation as a function of CWV and $\overline{T}$ (Neelin et al. 2009; Kuo et al. 2018).

## 5. Adjusting to QE

When convectively tranquil conditions are thermodynamically perturbed, convection responds by relaxing the perturbed environment to an adjusted state. The final adjusted state is not necessarily the same as the initial unperturbed state. How are these adjusted states

related to each other? How long does it take to accomplish the adjustment? In this section, we examine how the adjusted state and the convective adjustment process are related to each other and to the sensitivity time scales derived in the preceding section.

### a. Base-state trade-offs

The pdf of $B_L$ in Fig. 2 indicates that positive excursions in $B_L$ are consumed rapidly, and the mode of the $B_L$ pdf peaks close to $B_c$—implying that negative excursions in $B_L$ are also consumed, though not as rapidly. Tropical base states in precipitating regimes are therefore characterized such that their $B_L \approx B_c$; that is, they fluctuate about an adjusted QE state. Multiple combinations of $e_B$, $q_L$ and $T_L$ can yield the same value of $B_c$. The QE state is, therefore, not a single point in the three-dimensional space spanned by $e_B$, $q_L$, and $T_L$, but a set of points that constitute a two-dimensional surface. When $e_B$, $q_L$, and $T_L$ are modified by perturbations external to convection, they are constrained to evolve toward the QE state. We explore some straightforward implications of this constraint for how the adjusted QE state varies with convection's sensitivity to moisture and temperature.

We work with $\theta_e$ variables in lieu of moist enthalpy. Since the adjusted QE state also corresponds to the most probable state, it can be interpreted as the mean state or the base state. Consider two adjusted (or base) states, such that

$$B_L = B_c(\theta_{eB1}, \theta_{eL1}, \theta^*_{eL1}) = B_c(\theta_{eB2}, \theta_{eL2}, \theta^*_{eL2}),$$

where the two base states have different combinations of $\theta_{eB}$, $\theta_{eL}$, and $\theta^*_{eL}$, differentiated by subscripts 1 and 2. Using (2) and (3), we can write

$$[(\theta_{eB1} - \theta^*_{eL1}) - (\theta_{eB2} - \theta^*_{eL2})] = \frac{(1 - w_B)}{w_B}(\theta^+_{eL1} - \theta^+_{eL2}), \tag{32}$$

where we have assumed negligible differences between $\theta^*_{eL1}$ and $\theta^*_{eL2}$, when they appear in the denominator. Recall that $w_B$ and $w_L = 1 - w_B$ are the contributions of the CAPE-like quantity and the subsaturation components to $B_L$, respectively. Larger values of $w_L$ imply greater influence from the subsaturation term and therefore increased entrainment in the lower free troposphere. Comparing (2) and (32) makes it clear that base states in QE exhibit compensations between CAPE and subsaturation contributions, with the degree of compensation modulated by the extent of entrainment. With substantial entrainment, ($w_B < 0.5 \Leftrightarrow w_L > 0.5$), a given change in subsaturation elicits greater changes in CAPE. Moreover, when boundary layer $\theta_e$ is relatively constant, changes in the CAPE-like quantity would be associated with changes in static stability. The result (32) therefore connects with findings from Singh and O'Gorman (2013), who explored entrainment impacts on the static stability of different base states (see their Fig. 3), and also with lower-tropospheric moisture–static stability relationships termed moisture quasi equilibrium (Raymond et al. 2015; Sessions et al. 2019).

Now, consider three special cases for $w_B$:

1) $w_B = w_L = 0.5$. These values of $w_B$ and $w_L$ correspond to entrainment prescribed by a deep-inflow mass-flux profile for the assumed layer depths in section 2, and have empirical support (AN18; Schiro et al. 2018). With these values for $w_L$ and $w_B$, condition (32) gives

$$(\theta_{eB1} - \theta^*_{eL1}) - (\theta_{eB2} - \theta^*_{eL2}) = \theta^+_{eL1} - \theta^+_{eL2}. \tag{33}$$

   In this case, base states evolve such that changes to their lower-free-tropospheric subsaturation are cancelled by equally opposite changes to the base-state undilute buoyancy.
2) $w_B = 1$ (nonentraining): This condition implies negligible entrainment in the lower free troposphere, so $B_L$ is completely determined by the differences between boundary layer $\theta_e$ and the lower-free-tropospheric $\theta^*_e$, that is, by the CAPE-like term. The condition (32) now yields

$$\theta_{eB1} - \theta^*_{eL1} = \theta_{eB2} - \theta^*_{eL2}. \tag{34}$$

   In this nonentraining case, increases in boundary layer $\theta_e$ are exactly cancelled by increases in lower-free-tropospheric $\theta^*_e$. Comparing (34) to (2), we see that the undilute plume buoyancy (CAPE) remains unchanged between adjusted states. If we additionally assume that $B_c = 0$, we get $\theta_{eB1} = \theta^*_{eL1}$, so base states simply maintain convective neutrality to reduce all positive $B_L$ perturbations.
3) $w_B = 0$: This condition implies heavy entrainment in the lower free troposphere, such that the influence of CAPE on $B_L$ vanishes. The condition (32) now reduces to

$$\theta^+_{eL1} = \theta^+_{eL2}. \tag{35}$$

In the heavily entraining case, base states simply maintain the same subsaturation, while the lapse rates are unconstrained by convection. This condition further implies that warmer base states will hold more moisture in the lower free troposphere, exactly in accordance with the Clausius–Clapeyron relationship. If we further assume that $B_c = 0$, then we get $\theta_{eL} = \theta^*_{eL}$; that is,

convection maintains neutral buoyancy only when the lower free troposphere is saturated.

The degree of dilution by free-tropospheric air therefore constrains the thermodynamic properties of the adjusted states. In practice, case 2 is rarely encountered, while case 3 is never encountered. In climate models, the entrainment effects on deep convection are explicitly specified inside the deep convective scheme. Moreover, the convective adjustment within the deep convective schemes proceeds analogously to the $B_L$ adjustment. Despite the sensitivity of the climate model precipitation field to several parameters in the microphysics and shallow convective schemes (Qian et al. 2018), the cases discussed above are therefore still useful when interpreting aspects of mean state responses to entrainment experiments in these models (Mapes and Neale 2011; Kim et al. 2011, 2012).

### b. *Time scales of convective adjustment*

Within the foregoing framework, we can ask how the difference in convective sensitivity to moisture versus temperature perturbations determines the transient character of convective adjustment, including a single time scale for the adjustment of $B_L$. Consider the simple system (23) and (24), without the source or transport terms, which gives

$$\left(\frac{\partial \hat{q}}{\partial t}\right)_c = -\hat{Q}_c, \tag{36}$$

$$\left(\frac{\partial \hat{T}}{\partial t}\right)_c = \hat{Q}_c, \tag{37}$$

where the subscript $c$ clarifies our interest in how convection reacts to external perturbations. Note that $\hat{Q}_c$ here subsumes the effects of all the processes that contribute to condensational heating including microphysical changes, eddy transports, and downdrafts.

We will use (30) to represent $\hat{Q}_c$. Consider perturbations, $\hat{q}' = \hat{q} - \hat{q}_c$ and $\hat{T}' = \hat{T} - \hat{T}_c$, such that $B_L(\hat{q}, \hat{T}) > B_c(\hat{q}_c, \hat{T}_c)$. Assuming that both $\hat{q}'$ and $\hat{T}'$ exponentially decay with a convective adjustment time scale $\lambda^{-1}$ sets up a simple eigenvalue problem:

$$\left(\lambda + \frac{1}{\tilde{\tau}_q}\right)\hat{q}' - \frac{\hat{T}'}{\tilde{\tau}_t} = 0, \tag{38}$$

$$\frac{\hat{q}'}{\tilde{\tau}_q} - \left(\lambda + \frac{1}{\tilde{\tau}_t}\right)\hat{T}' = 0. \tag{39}$$

The constraint of nontrivial solutions to $\hat{q}'$ and $\hat{T}'$ yield two eigenvalues, $\lambda_1$ and $\lambda_2$, and the conditions satisfied by their respective eigenvectors:

$$\lambda_1 = 0; \quad \frac{\hat{q}'}{\tilde{\tau}_q} = \frac{\hat{T}'}{\tilde{\tau}_t}, \tag{40}$$

$$\lambda_2 = -\left(\frac{\tilde{\tau}_q + \tilde{\tau}_t}{\tilde{\tau}_q \tilde{\tau}_t}\right); \quad \hat{q}' = -\hat{T}'. \tag{41}$$

Conditions (40) and (41) yield more insight into the adjustment process. In a two dimensional plane spanned by $\hat{q}$ and $\hat{T}$ (the $\hat{q}$–$\hat{T}$ plane), we observe that:

1) The first eigenvector points in the direction of zero precipitation—from (30). This simply corresponds to the line containing all adjusted states. So the first eigenvalue-eigenvector pair in (40) makes the observation that there is no adjustment when $B_L = B_c$.
2) The second eigenvector in (41) points in a direction that conserves column-integrated MSE, and thus consumes both $\hat{T}'$ and $\hat{q}'$ at the same rate, given by $\lambda_2$. This direction has a slope $= -1$, which implies that drying coincides with warming.

Despite convection's greater sensitivity to temperature perturbations, both column-integrated temperature and moisture anomalies are consumed at the same rate. This is because convective tendencies are subject to the additional constraint that column-integrated latent heating must balance the column-integrated drying due to phase change, or in other words, the column-integrated MSE must be conserved during adjustment. The time scale of convective adjustment, $\tau_c = -\lambda_2^{-1}$, is a combination of individual convective sensitivities $\tilde{\tau}_q$ and $\tilde{\tau}_t$:

$$\tau_c = \frac{\tilde{\tau}_q \tilde{\tau}_t}{\tilde{\tau}_q + \tilde{\tau}_t}. \tag{42}$$

Entirely disregarding convection's sensitivity to temperature ($\tilde{\tau}_t \to \infty$), yields $\tau_c = \tilde{\tau}_q$; that is, the convective moisture sensitivity is also the convective adjustment time. For both sets of $\tilde{\tau}_q$ and $\tilde{\tau}_t$ values described in section 4, $\tau_c \approx 2$ h. The large temperature sensitivity of $B_L$, therefore, constrains the convective adjustment time to be short, that is, on the order of a few hours. Our result is consistent with Raymond and Herman (2011), who suggested that the large lower-tropospheric temperature sensitivity of convection and moist entropy conservation implied the same rapid consumption time scale for both lower-tropospheric temperature and moisture.

Figure 4 depicts how the $B_L$ adjustment proceeds in $\hat{q}$–$\hat{T}$ plane. In this two-dimensional plane, the set of $\hat{q}$ and $\hat{T}$ values for which $B_L = B_c$ lie on a straight line, which we term the "QE line." The QE line is dashed in

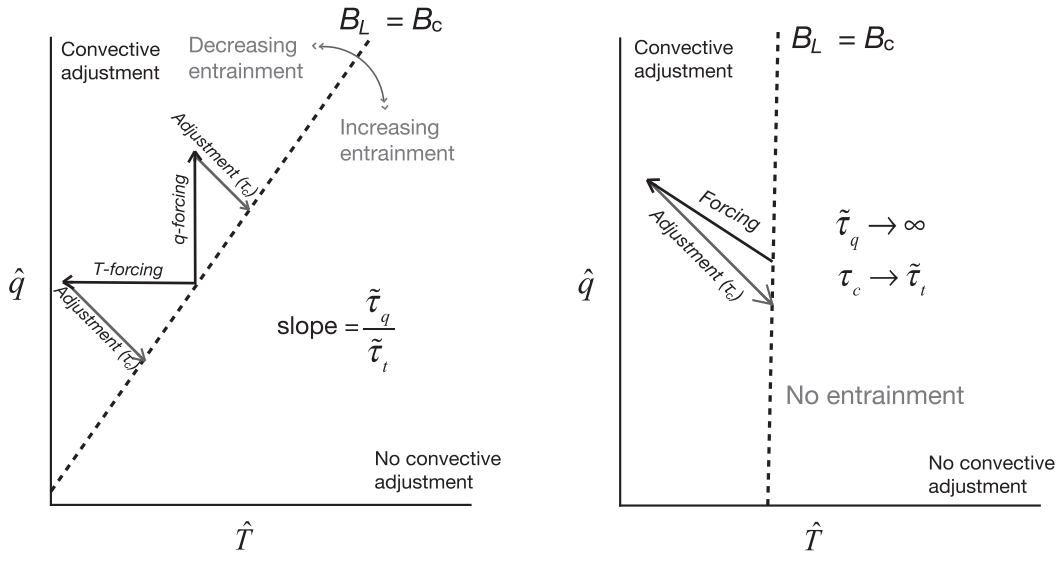


FIG. 4. A schematic adapted from Arakawa (2004) that depicts how convective adjustment proceeds in the $\hat{q}$–$\hat{T}$ plane. The dashed line is the QE line (31) that satisfies $B_L = B_c$ and its slope is governed by the ratio of the time-scale parameters characterizing moisture and temperature sensitivity. (left) A realistic entrainment case, and the adjustment associated with two positive buoyancy perturbations: one entirely in moisture ($q$-forcing) and the other in temperature ($T$ forcing). The adjustment occurs at a rate and direction given by (41). (right) Adjustment in response to an arbitrary forcing, in the limit of no entrainment. The angle of convective adjustment is the same for all three cases.

Fig. 4 and separates the $\hat{q}$–$\hat{T}$ plane into points that respond to a forcing with adjustment from those that do not. The left panel shows two equal and positive $B_L$ perturbations: one entirely in $\hat{q}$ ($q$-forcing) and the other entirely in $\hat{T}$ ($T$-forcing). Both forcings are adjusted to the QE line with the same time scale $\tau_c$. The angle of adjustment is $-45°$ with respect to the origin, and is *independent* of the forcing. The adjusted states in both cases are different from each other and also from the initial unperturbed state.

The slope of the QE line is given by the ratio of $\tilde{\tau}_q$ to $\tilde{\tau}_t$; changes to this slope impact the relationships between adjusted states. For instance, consider the case when $w_b \to 1$, that is, the nonentraining case. Also assume that the boundary layer moisture content is assumed fixed, such that convection is not sensitive to perturbations in the column-integrated moisture, that is, $\tilde{\tau}_q \to \infty$. The QE line in this case is nearly vertical in the $\hat{q}$–$\hat{T}$ plane (right panel in Fig. 4). This vertical QE line also features in Sahany et al. (2012) for plume calculations with low entrainment. The upper bound of $\hat{q}$ is fixed by the saturation value, which will restrict the range of $\hat{q}$ values usually encountered in the $\hat{q}$–$\hat{T}$ plane. For temperature perturbations with a fixed vertical profile, the constant $\hat{T}$ line also preserves the lapse rate, and this case reduces to case 2 discussed in section 5a. Changes to the moisture sensitivity of convection, that is, the entrainment parameter, therefore *influence the adjusted states by modifying the slope of the QE line*.

The schematic in Fig. 5 elaborates the differences in the adjustment process to separate moisture and temperature perturbations. Temperature perturbations impact plume buoyancy by modifying both the ambient static stability and the subsaturation, whereas moisture perturbations only change the subsaturation. The ensuing convection responds to both perturbations with a buoyancy adjustment that involves both temperature and moisture components and produces an adjusted state that is different from the unperturbed state. The final adjusted state, while always on the QE line, can correspond to a combination of $\hat{T}$ and $\hat{q}$ values that is different from the initial state. Here, the differences between initial and final states are governed by the convection's moisture and temperature sensitivities, $\tilde{\tau}_q$ and $\tilde{\tau}_t$, respectively.

It is worth bearing in mind that while positive buoyancy perturbations are consumed by convection, the ultimate fate of these perturbations is subject to the collective action of both convective and nonconvective processes. The convective adjustment process can interact with dynamical feedbacks through the transport terms to produce rich behavior (e.g., Neelin and Yu 1994; Sobel and Gildor 2003; Fuchs and Raymond 2005; Ahmed and Neelin 2019). A follow-up study will examine such interactions in greater detail.

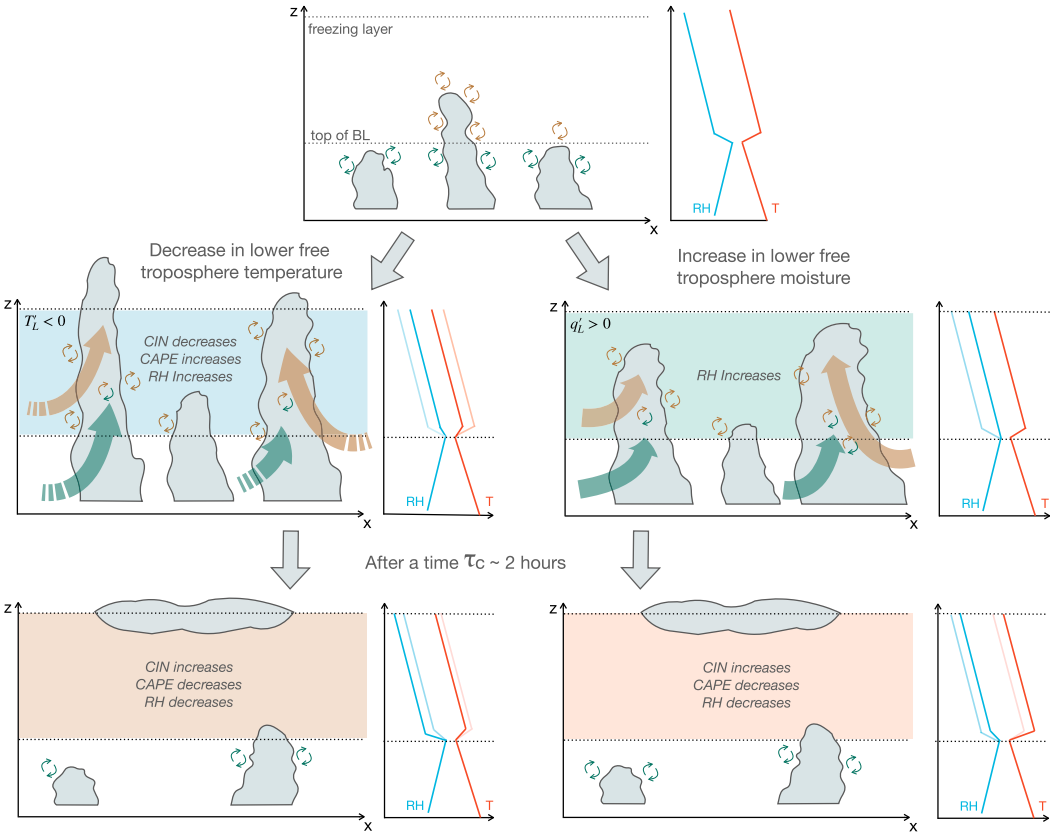


FIG. 5. A schematic depicting convective adjustment in response to moisture and temperature perturbations in the lower free troposphere. (top) The reference sounding responds to (middle left) temperature perturbations with changes to both the ambient subsaturation and lapse rate. (middle right) An equivalent perturbation in moisture only impacts the subsaturation. In both cases, the convective adjustment has the same time scale of $\tau_c \sim 2$ h. (bottom) The two adjusted states are, however, different from the initial sounding and from each other. The difference between initial and final adjusted states is governed by the slope of the QE line (Fig. 4). The initial sounding is rendered transparent in the middle and bottom rows.

### c. *Buoyancy removal time scale*

Many present-day mass-flux-based cumulus parameterization schemes rely on a closure based on APE or plume buoyancy removal (see section 5b in Arakawa 2004). To develop an analogous time scale for $B_L$ removal, (36), (37), and (41) can be combined:

$$\frac{\partial \hat{Q}_c}{\partial t} = -\frac{\hat{Q}_c}{\tau_c}. \tag{43}$$

Since $\hat{Q}_c = \alpha B_L$, we now see that $\tau_c$ is also the $B_L$ adjustment time scale, when $B_L > B_c$. For realistic values of entrainment, we saw that $\tau_c \sim 2$ h, which is consistent with analogous values employed in cumulus parameterization closures. The time scale $\tau_c$, derived from the slope of the empirical $P$–$B_L$ relationship in Fig. 2, remains invariant over a wide range of base states. However, the empirical dataset underlying our analysis is at $\sim 10^3$ km$^2$, with an estimated upper bound of $\sim 10^4$ km$^2$ for the spatial scales over which the derived value of $\tau_c$ is directly applicable. At larger spatial scales, the derived value of $\tau_c$ can still be used, provided that the neglected subgrid-scale variability is appropriately accounted for—as discussed in the following section.

## 6. Rectified adjustment time scales

### a. *Effects of averaging*

How can one reconcile the long adjustment times (>10 h) reported in several studies (Fuchs and Raymond 2002; Sobel and Bretherton 2003; Bretherton et al. 2004; Jiang et al. 2016; Adames 2017; Rushley et al. 2018) with shorter adjustment times (~2 h) reported in this study, recommended by Betts and Miller (1986), and used in cumulus parameterization schemes? Entirely neglecting convection's temperature sensitivity can lead to longer

adjustment times associated with moisture sensitivity only. However, such a neglect is only one source of discrepancy in reported $\tau_c$ values. We posit that another source of discrepancy lies in the use of spatiotemporally averaged data to compute adjustment times, which convolves events from both precipitating and nonprecipitating regimes. For simplicity, assume that the buoyancy fluctuations are primarily in moisture, with temperature held fixed at a large-scale value, as in the weak temperature gradient approximation (WTG; Sobel and Bretherton 2000; Sobel et al. 2001). Further assume that moisture fluctuations are vertically coherent, which then permits column-integrated moisture to be used as the main variable. The precipitation threshold in $B_L$ yields a temperature-dependent threshold value of column-integrated moisture, $\hat{q}_c$ above which precipitation increases linearly with moisture.

Consider a commonly used method to compute the adjustment times, in which precipitation is first conditionally averaged by column-integrated moisture, and then a time scale is estimated from the change in column-integrated moisture $\delta\overline{q}$ per unit change in precipitation $\delta\overline{P}$:

$$\tau_{\text{ave}} = \frac{\delta\overline{q}}{\delta\overline{P}}. \tag{44}$$

The overbar here refers to a spatiotemporal averaging operation. Assume that the data are spatially discrete and divided into grid cells. Within each grid cell, precipitation is assumed to remove $\hat{q}$ perturbations greater than $\hat{q}_c$ with a time scale $\tau_{\text{true}}$. Each grid cell is assumed to be sufficiently small that the results of our empirical analyses are applicable; that is, the grid cells are of order $10^3$ to at most $10^4\,\text{km}^2$. Grid cells with moisture perturbations such that $\hat{q} > \hat{q}_c$ will elicit responses in gridscale averaged precipitation, while cells with moisture perturbations such that $\hat{q} \le \hat{q}_c$, will not see a precipitation response. The averaging operation in (44) that produces $\tau_{\text{ave}}$, however, does not distinguish between precipitating and nonprecipitating grid cells in the sample, such that the apparent adjustment time, $\tau_{\text{ave}}$ will differ from $\tau_{\text{true}}$. For nonprecipitating grid cells, the adjustment time as implied by (44) is infinity. If $f$ is the fraction of precipitating grid cells (or grid cells experiencing convective adjustment), we can write $\delta q$ and $\delta\overline{P}$ from (44):

$$\delta\overline{q} \approx \delta(f\overline{q}_p) + \delta[(1-f)\overline{q}_{\text{np}}], \tag{45}$$

$$\delta\overline{P} \approx \overline{\overline{P}}\,\delta f + f\delta\overline{\overline{P}}\,, \tag{46}$$

where $\overline{q}_p$ and $\overline{q}_{\text{np}}$ are average moisture values over precipitating and nonprecipitating grid cells, respectively, and $\overline{\overline{P}}$ is the average rain over raining grid cells. We expand (45) as follows:

$$\delta\overline{q} \approx f\delta\overline{q}_p + (1-f)\delta\overline{q}_{\text{np}} + \delta f(\overline{q}_{\text{np}} - \overline{q}_p), \tag{47}$$

where $\delta f$ is the change in the fraction of precipitating grid cells. Using (46) and (47) in (44), we obtain

$$\tau_{\text{ave}} = C\left[\tau_{\text{true}} + \left(\frac{1-f}{f}\right)\tau_{\text{np1}} + \frac{\delta f}{f}\tau_{\text{np2}}\right], \tag{48}$$

where we have introduced the following definitions for three different time scales:

$$\tau_{\text{true}} = \frac{\delta\overline{q}_p}{\delta\overline{\overline{P}}},$$

$$\tau_{\text{np1}} = \frac{\delta\overline{q}_{\text{np}}}{\delta\overline{\overline{P}}},$$

$$\tau_{\text{np2}} = \frac{\overline{q}_p - \overline{q}_{\text{np}}}{\delta\overline{\overline{P}}},$$

where $\tau_{\text{true}}$ is the true moisture adjustment time, that is, the time scale associated with moisture removal via precipitation. The quantities $\tau_{\text{np1}}$ and $\tau_{\text{np2}}$ have units of time, but do not describe the *convective* adjustment process. They relate the moisture changes in the nonprecipitating grid cells to the precipitation change, and likely depend on details of moisture transport. We have also defined a dimensionless coefficient $C$:

$$C = \left(1 + \frac{\delta f}{f}\frac{\overline{\overline{P}}}{\delta\overline{\overline{P}}}\right)^{-1}. \tag{49}$$

This constant $C$ varies with the fraction of nonprecipitating grid cells in the averaging sample. In dry environments, $C < 1$. In moist environments, as $f \to 1$, the change in the fraction of precipitating grid cells, $\delta f \to 0$, which implies that $C \to 1$.

The time scale implied by $\tau_{\text{ave}}$, therefore, contains contributions from $\tau_{\text{true}}$, $\tau_{\text{np1}}$, and $\tau_{\text{np2}}$. For a significant fraction of nonprecipitating grid cells in the sample, $\tau_{\text{ave}}$ can be considerably longer than $\tau_{\text{true}}$. For samples with a greater fraction of precipitating grid cells; that is, as $f \to 1$, $\tau_{\text{ave}}$ will approach $\tau_{\text{true}}$. When (44) is used with data averaged over time scales longer than the true adjustment time, the resulting value is a rectified time scale that contains information about both the convective adjustment and the fraction of nonprecipitating grid cells in the spatiotemporal averaging interval.

### b. *Validation with a stochastic model*

To demonstrate the validity of the statements pertaining to spatiotemporal averaging and the effects of neglected influences on precipitation, we present analysis

from a simple stochastic model of tropical precipitation. Variants of this model have featured in several prior works (Stechmann and Neelin 2011, 2014; Abbott et al. 2016; Neelin et al. 2017; Martinez-Villalobos and Neelin 2019), so only a brief description is provided here. This model contains a single prognostic equation for column-integrated moisture $\hat{q}$:

$$d\hat{q} = (E + \hat{q}\overline{D} - P)dt + \hat{q}\sigma_c \xi_c \, dt, \tag{50}$$

an Ornstein–Uhlenbeck (Gardiner 2004) equation for the stochastic term $\xi_c$:

$$d\xi_c = -\xi_c \frac{dt}{\tau_{\text{ac}}} + \frac{dW_t}{\tau_{\text{ac}}}, \tag{51}$$

and a BM-type closure for precipitation:

$$P = \frac{(\hat{q} - \hat{q}_c)}{\tau_{\text{true}}} H(\hat{q} - \hat{q}_c). \tag{52}$$

Here, $dW_t$ is the derivative of the Wiener process (i.e., Brownian motion; see Gardiner 2004), $E$ is the evaporation, $\overline{D}$ is a mean large-scale, upper-level divergence, and $P$ is the precipitation. The stochastic term, $\xi_c$ has amplitude $\sigma_c$ and an autocorrelation time scale $\tau_{\text{ac}}$. In the deterministic closure, (52), precipitation is entirely determined by the value of $\hat{q}$. The moisture adjustment time, $\tau_{\text{true}}$ is set to 2 h. The effects of unaccounted influences on precipitation (e.g., variations in the vertical structure) can be incorporated in the form of a stochastic term within the precipitation closure:

$$P_{\text{stoch}} = \frac{(\hat{q} - \hat{q}_c + \sigma_q \xi_q)}{\tau_{\text{true}}} H(\hat{q} - \hat{q}_c + \sigma_q \xi_q), \tag{53}$$

where $\xi_q$ is a stochastic term with amplitude $\sigma_q$ and the following evolution equation:

$$d\xi_q = -\xi_q \frac{dt}{\tau_{\text{ac}}} + \frac{dW_t}{\tau_{\text{ac}}}. \tag{54}$$

The other model parameters with their values are detailed in Table 2. The model is integrated using the Euler–Maruyama scheme, with a time step of 3 min for a duration of ~12 weeks. This model captures the principal statistics of tropical convection—including the relationship between conditionally averaged precipitation and $\hat{q}$.

The instantaneous precipitation conditionally averaged by $\hat{q}$ (black curve in Fig. 6a) shows a sharp increase near $\hat{q} = \hat{q}_c$ (60 mm); the slope of this curve is $0.5\,\text{h}^{-1}$ by design. When the precipitation is averaged over time, say on daily time scales, the sharpness of the pickup reduces (blue curve in Fig. 6a); this smoothing is consistent with the behavior noted in observations (Kuo et al. 2018; Wolding et al. 2020—implicit in their Fig. 8). The green dashed curve in Fig. 6a is the instantaneous precipitation conditionally averaged by $\hat{q}$, but generated from the stochastic precipitation closure, (53). This curve shows how the sharpness of the pickup can be reduced even on fast time scales if the moisture threshold $q_c$ varies stochastically due to neglected subgrid-scale influences on the gridscale precipitation.

TABLE 2. Parameters of the stochastic model in section 4.

| Quantity | Description | Value |
|---|---|---|
| $E$ | Surface evaporation | $0.15\,\text{mm h}^{-1}$ |
| $\overline{D}$ | Mean upper-level divergence | $7.2 \times 10^{-3}\,\text{h}^{-1}$ |
| $\tau_{\text{true}}$ | Moisture adjustment time | 2 h |
| $\tau_{\text{ac}}$ | Autocorrelation time in noise | 1 h |
| $\sigma_c$ | Amplitude of stochastic convergence | $0.05\,\text{s}^{-1/2}$ |
| $\sigma_q$ | Amplitude of stochastic moisture threshold | $3\,\text{mm s}^{1/2}$ |
| $\hat{q}_c$ | Threshold moisture that triggers precipitation | 60 mm |

The sharp instantaneous precipitation curve with a long linear regime is insensitive to the point of linearization. The smooth daily precipitation curve and the instantaneous precipitation curve with a stochastic threshold, in contrast, offer multiple points for linearization—a few of which are marked by red stars in Fig. 6a. When conditionally averaging by daily averaged $\hat{q}$, each bin can contain varying fractions of precipitating grid cells (Fig. 6b). This fraction increases from 0 to 1 as daily averaged $\hat{q}$ increases. This changing fraction of precipitating grid cells influences the adjustment times computed using (44). Figure 6c compares the adjustment times calculated using (44) and using the definition of $\tau_{\text{ave}}$ from (48). The $\tau$ values computed using these two methods differ slightly, but show the same general trend. The computed $\tau$ values tend to converge to the true built-in adjustment time $\tau_{\text{true}}$, as the fraction of precipitating grid cells tends toward 1, and as the influence of the nonprecipitating state diminishes. The fraction of nonprecipitating grid cells, $f$, explains why the computed adjustment time varies with the base state of linearization (Adames 2017), and why applying (44) to climate model output (Jiang et al. 2016) can yield considerably longer adjustment times than the APE removal time scales built into the model cumulus parameterization scheme. Note that an effect equivalent to spatiotemporal averaging can also be introduced at the fast temporal and small spatial scales, if factors besides $\hat{q}$ influence precipitation. These factors can be represented with a stochastically varying $\hat{q}_c$.

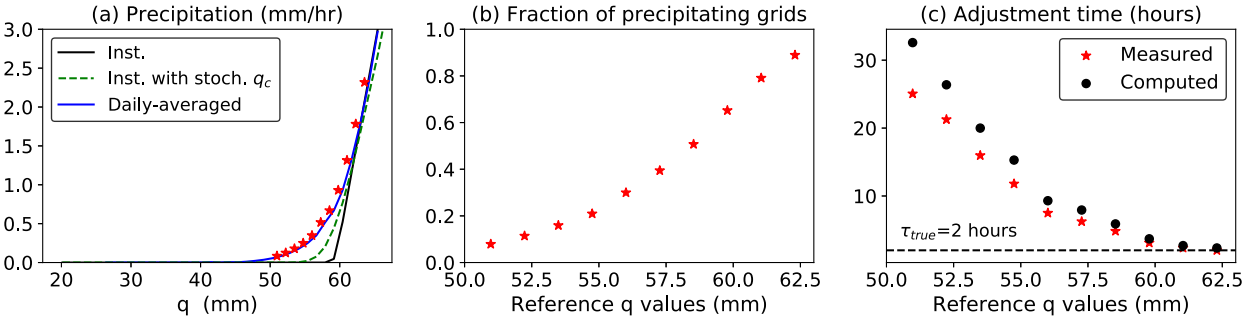


FIG. 6. (a) Conditionally averaged precipitation from a stochastic model of column-integrated moisture (see main text). Conditional averaging using instantaneous precipitation generated using a deterministic moisture threshold (black), a stochastic moisture threshold (green dashed line), and daily averaged precipitation using the deterministic precipitation threshold (blue). The red stars denote different reference values of CWV ($\hat{q}$). (b) The fraction of precipitating grid cells in the bins with a given reference $\hat{q}$ value. (c) The convective adjustment times measured numerically using (44) and computed analytically using (48) for each reference $\hat{q}$ value. The true adjustment time, built into the model precipitation closure, is indicated by the dashed horizontal line. Note the different $y$-axes ranges in (b) and (c).

From the arguments outlined in this section, we expect that using coarse-grained data to estimate adjustment time scales will yield values much longer than the underlying convective adjustment time scale. It is, however, important to distinguish the time scale representing the adjustment *process* from time scales more representative of averaging artifacts. This raises the question as to the optimal adjustment time scale that should be used in climate models operating on grids considerably coarser than our analysis scales ($\gtrsim 10^4 \text{km}^2$). Purely deterministic convective parameterization schemes might employ the longer apparent adjustment times. This approach, however, implies the use of nonunique adjustment times that vary with the subgrid-scale nonprecipitating fraction, as suggested by (48). A more straightforward way to handle the effects of neglected subgrid-scale variability is to use the short adjustment time, $\tau_{\text{true}}$, in conjunction with a stochastic precipitation closure (e.g., Lin and Neelin 2003). This is consistent with the notion that a single time scale characterizes the convective response, but its influence on the gridscale properties can be altered by unaccounted subgrid-scale fluctuations.

### c. *Temporally averaging the $P$–$B_L$ relationship*

In Fig. 7, the left panel compares the $P$–$B_L$ relationship with precipitation–column relative humidity ($P$–$r$) relationship. These figures were constructed using the same ERA-Interim and TRMM datasets introduced in section 2. The precipitation increase in the $P$–$B_L$ relationship is abrupt, when compared to the smoother increase seen in the $P$–$r$ relationship. The maximum value of conditionally averaged precipitation in the $P$–$B_L$ relationship ($\sim 5\,\text{mm}\,\text{h}^{-1}$) is also larger than in the $P$–$r$ relationship ($\sim 2\,\text{mm}\,\text{h}^{-1}$). Estimates of adjustment time using these relationships will remain robust when using the linear portion of the curves. The $P$–$B_L$ relationship has a longer linear portion, and a smaller "foot" region: the smooth portion connecting the linear portion to nonprecipitating points. The $P$–$r$ relationship, in contrast, has a smaller linear portion. So estimates of adjustment time scales from the $P$–$r$ relationship will run into issues of robustness, as demonstrated in sections 6a and 6b.

In the right panel of Fig. 7, the *instantaneous* $P$–$B_L$ relationship—so called because the ERA-Interim and TRMM 3B42 samples are nominal snapshots—shows the longest linear range. The length of this linear portion of the $P$–$B_L$ relationship clearly recedes with time averaging. With only four samples available per day, the effects of averaging are apparent only for intervals longer than 5 days (20 samples). The curvature near the "foot" region increases substantially as the linear portion of the $P$–$B_L$ relationship is completely averaged away for the 10-day and monthly time scales. Therefore, estimates of adjustment times, even when using the $P$–$B_L$ relationship, are sensitive to temporal averaging. Using near-instantaneous or short time-interval (hourly or less) data is expected to provide more accurate estimates of convective adjustment time scales.

It is interesting to consider why the $P$–$B_L$ relationship exhibits a sharper pickup than the $P$–$r$ relationship. Column relative humidity $r$ does not necessarily have a one-to-one relationship with $B_L$, so conditionally averaging on $r$ includes points with different values of $B_L$. This effect can be interpreted as a consequence of using a stochastic $r$ threshold for precipitation. The stochastic effects enter through variations present in $B_L$ that affect precipitation, but are not tracked by $r$. The result—as in the case of temporal averaging—is an increase in the curvature near the foot region.

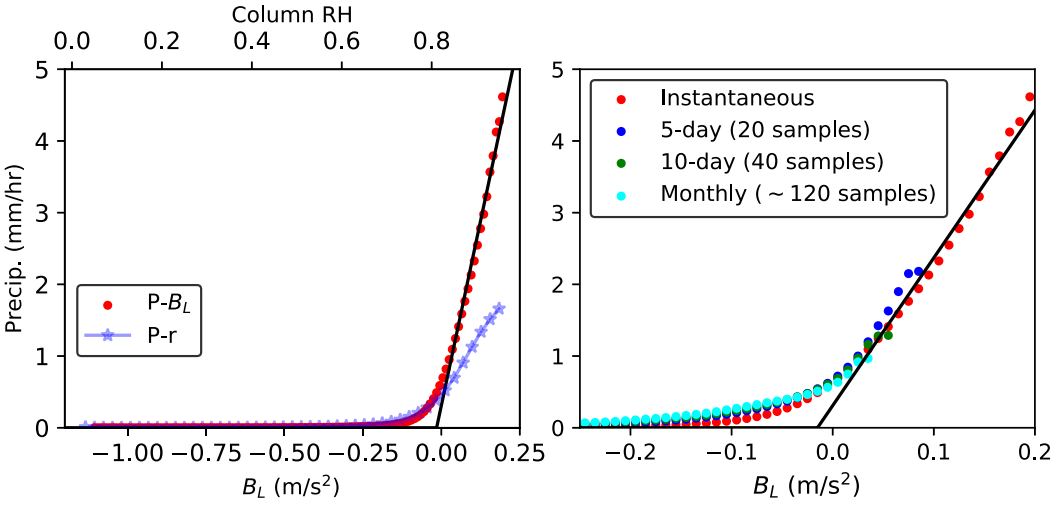


FIG. 7. (left) The relationship between precipitation conditionally averaged by $B_L$ (solid red scatter), and by column relative humidity (starred blue line). $B_L$ varies on the bottom $x$-axis, while column relative humidity varies on the top $x$-axis. (right) A zoomed-in view of the precipitation–$B_L$ relationship illustrating the effects of time averaging. The number of available samples for each interval are indicated within parentheses. In both panels, the black line has slope $\alpha$ (as in Fig. 3).

## 7. Summary and discussion

### a. Summary

The empirical precipitation–buoyancy relationship exhibits a substantial range over which it is approximately linear. Linearizing analytic expressions for this buoyancy in terms of equivalent potential temperature or moist enthalpy yields a relationship between precipitation perturbations and corresponding perturbations in thermodynamic properties of the boundary layer and the lower free troposphere (free troposphere below the freezing level). These precipitation sensitivities are expressed as time scale parameters, although the way these parameters combine to yield actual time scales depends on a number of interactions. Tropical precipitation is more sensitive to lower-free-tropospheric temperature perturbations—with an associated time scale parameter ~3 h—than to equivalent lower-free-tropospheric moisture or boundary layer moist enthalpy perturbations, with time scale parameters ~11 h. The differences in these sensitivities are attributed to the physical pathways through which each thermodynamic perturbation affects buoyancy. Temperature fluctuations affect convection through two pathways (change in undilute buoyancy and dilution), versus the one pathway available each for lower-free-tropospheric moisture (dilution) and boundary layer moist enthalpy effects (change in undilute buoyancy).

A simple precipitation closure ($q$–$T$ closure) that is suitable for use with both simple, linearized and nonlinear, intermediate-complexity tropical models is constructed from the empirical relationships. The $q$–$T$ closure is used to examine how column-integrated moisture ($\hat{q}$) and temperature ($\hat{T}$) perturbations are consumed by convection. Both perturbations are consumed at the same fast time scale (~2 h), and are relaxed to one among a continuum of adjusted states. The difference in convection's sensitivity to moisture versus temperature decides which adjusted state a given perturbation is relaxed to. These adjusted states are constrained such that in a relative sense: moist adjusted states are more stable and dry adjusted states are more unstable. Previous estimates that arrive at long moisture adjustment times may be attributing convective adjustment to regimes not actively experiencing adjustment. Increases in the fraction of nonprecipitating samples in the averaging interval is shown to lengthen adjustment times. This effect can be particularly acute when using spatiotemporally averaged data to estimate adjustment times, but can also result from neglected environmental influences on precipitation.

### b. Implications for convective quasi equilibrium

The empirical buoyancy-based framework constructs an analog ($B_L$) for similar buoyancy-based measures of convective instability in cumulus parameterization schemes; for example, the cloud work function (Arakawa and Schubert 1974) or CAPE (Zhang and McFarlane 1995; Neale et al. 2008). Observations (AN18; Schiro et al. 2018) suggest that $B_L$ is consumed—with ensuing precipitation—when it exceeds a threshold. These empirical results are consistent with the QE

hypothesis for deep convection (Arakawa and Schubert 1974; Emanuel et al. 1994; Neelin et al. 2008; Yano and Plant 2012). A number of studies have recognized that QE is a continuum of states (Arakawa 2004), set by trade-offs between the influence of temperature and moisture profiles on conditional instability. These effects have been quantified in a variety of ways in observations and models (Kuang 2008a; Neelin et al. 2009; Holloway and Neelin 2009; Sahany et al. 2012; Raymond and Herman 2011; Raymond et al. 2015; Kuo et al. 2018; Sessions et al. 2019). It is by now quite clear that the diluting effects of entrained subsaturated air must form a central ingredient (Neale et al. 2008; Zhang 2009) in the buoyancy measure being consumed. The analytic expressions (in section 5) show that the same sensitivity parameters that combine to govern the adjustment time scale also determine the QE line in the moisture–temperature plane. They clarify that the QE state does not correspond to a particular value of subsaturation. This is because temperature effects enter buoyancy by not only modifying the ambient saturation, but also by modifying the ambient thermal stratification. Column relative humidity is therefore a suboptimal measure of the thermodynamic environment for evaluating precipitation relations.

### c. *Entrainment and mean state degradation*

It is well known when entrainment is increased in climate models, the precipitation variance increases at the expense of mean state departures from observations (Mapes and Neale 2011; Kim et al. 2011, 2012). This property of climate models can be interpreted within the empirical buoyancy-based framework. In this framework, increasing the entrainment (and dilution) is tantamount to reducing $w_B$. As discussed in section 5a, this change increases the influence of ambient subsaturation, and decreases the influence of stratification on $B_L$. The large variance of the free-tropospheric moisture can therefore be translated into increased precipitation variance. In cumulus parameterization schemes, buoyancy measures such as CAPE or cloud work function are adjusted to a reference value close to zero. To satisfy the condition, $B_c = 0$, environments with no entrainment ($w_B = 1$) must attain lower-free-tropospheric convective neutrality ($\theta_{eB} = \theta^*_{eL}$), whereas environments with heavy entrainment ($w_B = 0$) must saturate the lower free troposphere ($\theta^+_{eL} = 0$). Therefore, as the entrainment parameter is varied from minimum to maximum values, the mean state, that is, the QE state to which convection adjusts the precipitating environment, correspondingly varies between neutral lapse rates and saturation in the lower free troposphere. Modifying entrainment can alternatively be viewed as increasing $\tau_q$, and thereby altering the slope of the QE line in Fig. 4. The same external perturbation is therefore adjusted to very different points on the QE line, depending on the value of entrainment.

Past work modifying entrainment in climate models (Kim et al. 2012) has also demonstrated trade-offs in variance between the convectively coupled Kelvin wave and the MJO. Several models simulate strong Kelvin wave variability and little MJO variability, and vice versa (Lin et al. 2006; Hung et al. 2013). Furthermore, several studies have found that models that simulate strong MJO variability exhibit more humid mean states (Kim 2017; Gonzalez and Jiang 2017). The MJO is thought to emerge from moisture fluctuations (Raymond 2001; Raymond and Fuchs 2009; Sobel and Maloney 2013; Adames and Kim 2016), and Kelvin waves from temperature fluctuations (Khouider and Majda 2006; Raymond and Fuchs 2007; Kuang 2008b; Herman et al. 2016). In the buoyancy framework, the degree of entrainment controls the ease with which precipitation can be triggered by moisture versus temperature fluctuations; precipitation is more easily triggered by temperature fluctuations when entrainment is small and vice versa. The buoyancy framework developed here, therefore, offers a starting point for future explorations related to entrainment-induced trade-offs in MJO–Kelvin wave precipitation variance.

### d. *Adjustment-based closures and their applicability*

The adjustment to QE occurs in strongly precipitating conditions, that is, in environments where $B_L \geq B_c$. Under these conditions, positive buoyancy fluctuations are damped rapidly—as also attested to by observational studies (Masunaga 2012; Hohenegger and Stevens 2013). However, as seen in Fig. 4, the QE line is only the boundary separating convectively damped and undamped tropical environments. The undamped environments include dry, subsiding regions that pervade much of the tropics and sit away from QE. In such regions, the dominant time scales are controlled by other processes (Masunaga and Mapes 2020): radiatively induced subsidence, gradual moistening through shallow and congestus clouds, advective transport and surface fluxes, for which it may not be meaningful to speak of convective adjustment time scales.

It is worth highlighting that the adjustment process here is estimated from conditional mean precipitation, and that there will always be fluctuations away from QE, arising from both variations in large-scale dynamical transports and fluctuations in the convection itself. These variations from QE yield important qualities such as the probability distribution of

precipitation accumulations, intensities, durations, and clusters (e.g., Stechmann and Neelin 2014; Neelin et al. 2017; Martinez-Villalobos and Neelin 2018, 2019; Ahmed and Neelin 2019). The adjustment time scales are important to the amplitude of such fluctuations and to the resulting precipitation-related distributions. In climate models, these fluctuations can be captured with prescribed stochastic variability in cumulus parameterization schemes (Lin and Neelin 2003; Plant and Craig 2008; Khouider et al. 2010; Hagos et al. 2018). Moreover, the effects of spatiotemporal averaging on precipitation statistics suggest that the stochastic variability must scale with the horizontal grid size, precluding the need for spatiotemporally varying adjustment time scales in climate models.

The results in this study also highlight the difference between sensitivity of convection to a particular thermodynamic forcing, and the time scale characterizing the convective response. Inferring one quantity from the other must account for distorted causality between forcing and adjustment (Mapes et al. 2019). The time scale of convective adjustment will tend to be dominated by the more sensitive variable, that is, temperature. Neglecting temperature contributions to precipitation adjustment therefore produces longer estimates for $\tau_c$. Neglected temperature contributions also imply neglected precipitation variance—particularly in spatiotemporal windows that host convectively coupled Kelvin and gravity waves. It is nevertheless interesting to consider situations in which the temperature contribution to precipitation adjustment can be justifiably omitted. One obvious possibility is under the constraint of WTG: when temperature perturbations are erased by gravity waves with either infinite (Sobel and Bretherton 2000; Sobel et al. 2001) or finite phase speeds (Raymond and Zeng 2005; Wang and Sobel 2011; Daleu et al. 2015). The latter case is particular interesting when considering how the short, but finite, gravity wave time scale will interact with the similarly short time scale parameters governing the temperature and moisture response to convection. A related follow-up study will use a simple, linearized model of tropical dynamics to explore how the constraints of QE and WTG interact with each other.

*Acknowledgments.* This research was supported by National Science Foundation Grants AGS-1540518, AGS-1936810 (F.A. and J.D.N.), and AGS-1841559 (Á.F.A.). Discussions with Brian Mapes, Cristian Martinez-Villalobos, and Jesse Norris and comments from two anonymous reviewers helped improved aspects of this paper.

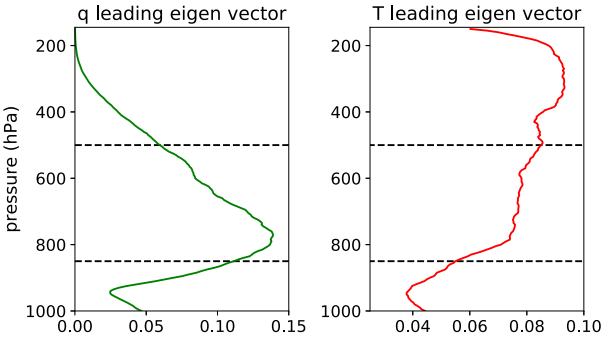


FIG. A1. The leading eigenvectors of (left) moisture and (right) temperature variations as computed from a time series of radiosonde data from the ARM site at Nauru. The horizontal lines demarcate the boundary layer (1000–850 hPa) and the lower-free troposphere (850–500 hPa). These vertical structures are used to transform the adjustment times for vertically averaged moisture and temperature into adjustment times for column integrals in section 4.

## APPENDIX

### Vertical Structures of Moisture and Temperature

Figure A1 shows the first EOFs of moisture and temperature variations computed from a radiosonde time series.

## REFERENCES

Abbott, T. H., S. N. Stechmann, and J. D. Neelin, 2016: Long temporal autocorrelations in tropical precipitation data and spike train prototypes. *Geophys. Res. Lett.*, **43**, 11 472–11 480, https://doi.org/10.1002/2016GL071282.

Adames, Á. F., 2017: Precipitation budget of the Madden–Julian oscillation. *J. Atmos. Sci.*, **74**, 1799–1817, https://doi.org/10.1175/JAS-D-16-0242.1.

——, and J. M. Wallace, 2014: Three-dimensional structure and evolution of the MJO and its relation to the mean flow. *J. Atmos. Sci.*, **71**, 2007–2026, https://doi.org/10.1175/JAS-D-13-0254.1.

——, and D. Kim, 2016: The MJO as a dispersive, convectively coupled moisture wave: Theory and observations. *J. Atmos. Sci.*, **73**, 913–941, https://doi.org/10.1175/JAS-D-15-0170.1.

——, and Y. Ming, 2018: Interactions between water vapor and potential vorticity in synoptic-scale monsoonal disturbances: Moisture vortex instability. *J. Atmos. Sci.*, **75**, 2083–2106, https://doi.org/10.1175/JAS-D-17-0310.1.

——, D. Kim, S. K. Clark, Y. Ming, and K. Inoue, 2019: Scale analysis of moist thermodynamics in a simple model and the relationship between moisture modes and gravity waves. *J. Atmos. Sci.*, **76**, 3863–3881, https://doi.org/10.1175/JAS-D-19-0121.1.

Ahmed, F., and C. Schumacher, 2015: Convective and stratiform components of the precipitation-moisture relationship. *Geophys. Res. Lett.*, **42**, 10 453–10 462, https://doi.org/10.1002/2015GL066957.

——, and ——, 2017: Geographical differences in the tropical precipitation-moisture relationship and rain intensity onset. *Geophys. Res. Lett.*, **44**, 1114–1122, https://doi.org/10.1002/2016GL071980.

——, and J. D. Neelin, 2018: Reverse engineering the tropical precipitation–buoyancy relationship. *J. Atmos. Sci.*, **75**, 1587–1608, https://doi.org/10.1175/JAS-D-17-0333.1.

——, and ——, 2019: Explaining scales and statistics of tropical precipitation clusters with a stochastic model. *J. Atmos. Sci.*, **76**, 3063–3087, https://doi.org/10.1175/JAS-D-18-0368.1.

Arakawa, A., 2004: The cumulus parameterization problem: Past, present, and future. *J. Climate*, **17**, 2493–2525, https://doi.org/10.1175/1520-0442(2004)017<2493:RATCPP>2.0.CO;2.

——, and W. H. Schubert, 1974: Interaction of a cumulus cloud ensemble with the large-scale environment, part I. *J. Atmos. Sci.*, **31**, 674–701, https://doi.org/10.1175/1520-0469(1974)031<0674:IOACCE>2.0.CO;2.

Bechtold, P., M. Köhler, T. Jung, F. Doblas-Reyes, M. Leutbecher, M. J. Rodwell, F. Vitart, and G. Balsamo, 2008: Advances in simulating atmospheric variability with the ECMWF model: From synoptic to decadal time-scales. *Quart. J. Roy. Meteor. Soc.*, **134**, 1337–1351, https://doi.org/10.1002/QJ.289.

Bernstein, D. N., and J. D. Neelin, 2016: Identifying sensitive ranges in global warming precipitation change dependence on convective parameters. *Geophys. Res. Lett.*, **43**, 5841–5850, https://doi.org/10.1002/2016GL069022.

Betts, A. K., 1986: A new convective adjustment scheme. Part I: Observational and theoretical basis. *Quart. J. Roy. Meteor. Soc.*, **112**, 677–691, https://doi.org/10.1002/QJ.49711247307.

——, and M. J. Miller, 1986: A new convective adjustment scheme. Part II: Single column tests using GATE wave, BOMEX, ATEX and Arctic air-mass data sets. *Quart. J. Roy. Meteor. Soc.*, **112**, 693–709, https://doi.org/10.1002/QJ.49711247308.

Boos, W. R., and T. Storelvmo, 2016: Near-linear response of mean monsoon strength to a broad range of radiative forcings. *Proc. Natl. Acad. Sci. USA*, **113**, 1510–1515, https://doi.org/10.1073/pnas.1517143113.

Bretherton, C. S., M. E. Peters, and L. E. Back, 2004: Relationships between water vapor path and precipitation over the tropical oceans. *J. Climate*, **17**, 1517–1528, https://doi.org/10.1175/1520-0442(2004)017<1517:RBWVPA>2.0.CO;2.

Bullock, O. R., K. Alapaty, J. A. Herwehe, and J. S. Kain, 2015: A dynamically computed convective time scale for the Kain–Fritsch convective parameterization scheme. *Mon. Wea. Rev.*, **143**, 2105–2120, https://doi.org/10.1175/MWR-D-14-00251.1.

Cohen, B. G., and G. C. Craig, 2004: The response time of a convective cloud ensemble to a change in forcing. *Quart. J. Roy. Meteor. Soc.*, **130**, 933–944, https://doi.org/10.1256/QJ.02.218.

Daleu, C. L., and Coauthors, 2015: Intercomparison of methods of coupling between convection and large-scale circulation: 1. Comparison over uniform surface conditions. *J. Adv. Model. Earth Syst.*, **7**, 1576–1601, https://doi.org/10.1002/2015MS000468.

Dee, D. P., and Coauthors, 2011: The ERA-Interim reanalysis: Configuration and performance of the data assimilation system. *Quart. J. Roy. Meteor. Soc.*, **137**, 553–597, https://doi.org/10.1002/qj.828.

Done, J. M., G. C. Craig, S. L. Gray, P. A. Clark, and M. E. B. Gray, 2006: Mesoscale simulations of organized convection: Importance of convective equilibrium. *Quart. J. Roy. Meteor. Soc.*, **132**, 737–756, https://doi.org/10.1256/qj.04.84.

Doswell, C. A., and P. M. Markowski, 2004: Is buoyancy a relative quantity? *Mon. Wea. Rev.*, **132**, 853–863, https://doi.org/10.1175/1520-0493(2004)132<0853:IBARQ>2.0.CO;2.

Emanuel, K. A., J. D. Neelin, and C. S. Bretherton, 1994: On large-scale circulations in convecting atmospheres. *Quart. J. Roy. Meteor. Soc.*, **120**, 1111–1143, https://doi.org/10.1002/qj.49712051902.

Ferrier, B. S., and R. A. Houze, 1989: One-dimensional time-dependent modeling of gate cumulonimbus convection. *J. Atmos. Sci.*, **46**, 330–352, https://doi.org/10.1175/1520-0469(1989)046<0330:ODTDMO>2.0.CO;2.

Frierson, D. M. W., 2007a: The dynamics of idealized convection schemes and their effect on the zonally averaged tropical circulation. *J. Atmos. Sci.*, **64**, 1959–1976, https://doi.org/10.1175/JAS3935.1.

——, 2007b: Convectively coupled Kelvin waves in an idealized moist general circulation model. *J. Atmos. Sci.*, **64**, 2076–2090, https://doi.org/10.1175/JAS3945.1.

Fuchs, Ž., and D. J. Raymond, 2002: Large-scale modes of a nonrotating atmosphere with water vapor and cloud–radiation feedbacks. *J. Atmos. Sci.*, **59**, 1669–1679, https://doi.org/10.1175/1520-0469(2002)059<1669:LSMOAN>2.0.CO;2.

——, and ——, 2005: Large-scale modes in a rotating atmosphere with radiative–convective instability and WISHE. *J. Atmos. Sci.*, **62**, 4084–4094, https://doi.org/10.1175/JAS3582.1.

——, and ——, 2007: A simple, vertically resolved model of tropical disturbances with a humidity closure. *Tellus*, **59A**, 344–354, https://doi.org/10.1111/j.1600-0870.2007.00230.x.

——, and ——, 2017: A simple model of intraseasonal oscillations. *J. Adv. Model. Earth Syst.*, **9**, 1195–1211, https://doi.org/10.1002/2017MS000963.

——, S. L. Sessions, and D. J. Raymond, 2014: Mechanisms controlling the onset of simulated convectively coupled Kelvin waves. *Tellus*, **66A**, 22107, https://doi.org/10.3402/tellusa.v66.22107.

Gardiner, C. W., 2004: *Handbook of Stochastic Methods for Physics, Chemistry and the Natural Sciences*. 3rd ed. Springer Series in Synergetics, Vol. 13, Springer-Verlag, 415 pp.

Gonzalez, A. O., and X. Jiang, 2017: Winter mean lower tropospheric moisture over the Maritime Continent as a climate model diagnostic metric for the propagation of the Madden-Julian oscillation. *Geophys. Res. Lett.*, **44**, 2588–2596, https://doi.org/10.1002/2016GL072430.

Hack, J. J., 1994: Parameterization of moist convection in the National Center for Atmospheric Research Community Climate Model (CCM2). *J. Geophys. Res.*, **99**, 5551–5568, https://doi.org/10.1029/93JD03478.

Hagos, S., Z. Feng, R. S. Plant, R. A. Houze Jr., and H. Xiao, 2018: A stochastic framework for modeling the population dynamics of convective clouds. *J. Adv. Model. Earth Syst.*, **10**, 448–465, https://doi.org/10.1002/2017MS001214.

Herman, M. J., Z. Fuchs, D. J. Raymond, and P. Bechtold, 2016: Convectively coupled Kelvin waves: From linear theory to global models. *J. Atmos. Sci.*, **73**, 407–428, https://doi.org/10.1175/JAS-D-15-0153.1.

Hersbach, H., and Coauthors, 2019: Global reanalysis: Goodbye ERA-Interim, hello ERA5. *ECMWF Newsletter*, No. 159, ECMWF, Reading, United Kingdom, 17–24.

Hohenegger, C., and B. Stevens, 2013: Preconditioning deep convection with cumulus congestus. *J. Atmos. Sci.*, **70**, 448–464, https://doi.org/10.1175/JAS-D-12-089.1.

Holloway, C. E., and J. D. Neelin, 2009: Moisture vertical structure, column water vapor, and tropical deep convection. *J. Atmos. Sci.*, **66**, 1665–1683, https://doi.org/10.1175/2008JAS2806.1.

Hottovy, S., and S. N. Stechmann, 2015: Threshold models for rainfall and convection: Deterministic versus stochastic triggers. *SIAM J. Appl. Math.*, **75**, 861–884, https://doi.org/10.1137/140980788.

Huffman, G. J., and Coauthors, 2007: The TRMM Multisatellite Precipitation Analysis (TMPA): Quasi-global, multiyear, combined-sensor precipitation estimates at fine scales. *J. Hydrometeor.*, **8**, 38–55, https://doi.org/10.1175/JHM560.1.

Hung, M.-P., J.-L. Lin, W. Wang, D. Kim, T. Shinoda, and S. J. Weaver, 2013: MJO and convectively coupled equatorial waves simulated by CMIP5 climate models. *J. Climate*, **26**, 6185–6214, https://doi.org/10.1175/JCLI-D-12-00541.1.

Igel, M. R., 2017: The tropical precipitation pickup threshold and clouds in a radiative convective equilibrium model: 2. Two-layer moisture. *J. Geophys. Res. Atmos.*, **122**, 6469–6487, https://doi.org/10.1002/2016JD025908.

——, S. R. Herbener, and S. M. Saleeby, 2017: The tropical precipitation pickup threshold and clouds in a radiative convective equilibrium model: 1. Column moisture. *J. Geophys. Res. Atmos.*, **122**, 6453–6468, https://doi.org/10.1002/2016JD025907.

Jiang, X., M. Zhao, E. D. Maloney, and D. E. Waliser, 2016: Convective moisture adjustment time scale as a key factor in regulating model amplitude of the Madden-Julian oscillation. *Geophys. Res. Lett.*, **43**, 10 412–10 419, https://doi.org/10.1002/2016GL070898.

Kain, J. S., 2004: The Kain–Fritsch convective parameterization: An update. *J. Appl. Meteor.*, **43**, 170–181, https://doi.org/10.1175/1520-0450(2004)043<0170:TKCPAU>2.0.CO;2.

Khouider, B., and A. J. Majda, 2006: A simple multicloud parameterization for convectively coupled tropical waves. Part I: Linear analysis. *J. Atmos. Sci.*, **63**, 1308–1323, https://doi.org/10.1175/JAS3677.1.

——, J. Biello, and A. J. Majda, 2010: A stochastic multicloud model for tropical convection. *Commun. Math. Sci.*, **8**, 187–216, https://doi.org/10.4310/CMS.2010.v8.n1.a10.

Kiladis, G. N., M. C. Wheeler, P. T. Haertel, K. H. Straub, and P. E. Roundy, 2009: Convectively coupled equatorial waves. *Rev. Geophys.*, **47**, RG2003, https://doi.org/10.1029/2008RG000266.

Kim, D., A. H. Sobel, E. D. Maloney, D. M. W. Frierson, and I.-S. Kang, 2011: A systematic relationship between intraseasonal variability and mean state bias in AGCM simulations. *J. Climate*, **24**, 5506–5520, https://doi.org/10.1175/2011JCLI4177.1.

——, ——, A. D. Del Genio, Y. Chen, S. J. Camargo, M.-S. Yao, M. Kelley, and L. Nazarenko, 2012: The tropical subseasonal variability simulated in the NASA GISS general circulation model. *J. Climate*, **25**, 4641–4659, https://doi.org/10.1175/JCLI-D-11-00447.1.

Kim, H.-M., 2017: The impact of the mean moisture bias on the key physics of MJO propagation in the ECMWF reforecast. *J. Geophys. Res. Atmos.*, **122**, 7772–7784, https://doi.org/10.1002/2017JD027005.

Kingsmill, D. E., and R. A. Houze, 1999: Thermodynamic characteristics of air flowing into and out of precipitating convection over the west Pacific warm pool. *Quart. J. Roy. Meteor. Soc.*, **125**, 1209–1229, https://doi.org/10.1002/qj.1999.49712555606.

Kuang, Z., 2008a: Modeling the interaction between cumulus convection and linear gravity waves using a limited-domain cloud system–resolving model. *J. Atmos. Sci.*, **65**, 576–591, https://doi.org/10.1175/2007JAS2399.1.

——, 2008b: A moisture-stratiform instability for convectively coupled waves. *J. Atmos. Sci.*, **65**, 834–854, https://doi.org/10.1175/2007JAS2444.1.

——, 2010: Linear response functions of a cumulus ensemble to temperature and moisture perturbations and implications for the dynamics of convectively coupled waves. *J. Atmos. Sci.*, **67**, 941–962, https://doi.org/10.1175/2009JAS3260.1.

Kuo, Y.-H., K. A. Schiro, and J. D. Neelin, 2018: Convective transition statistics over tropical oceans for climate model diagnostics: Observational baseline. *J. Atmos. Sci.*, **75**, 1553–1570, https://doi.org/10.1175/JAS-D-17-0287.1.

Lin, J.-L., and Coauthors, 2006: Tropical intraseasonal variability in 14 IPCC AR4 climate models. Part I: Convective signals. *J. Climate*, **19**, 2665–2690, https://doi.org/10.1175/JCLI3735.1.

Lin, J. W.-B., and J. D. Neelin, 2003: Toward stochastic deep convective parameterization in general circulation models. *Geophys. Res. Lett.*, **30**, 1162, https://doi.org/10.1029/2002GL016203.

Madden, R. A., and P. R. Julian, 1971: Detection of a 40–50 day oscillation in the zonal wind in the tropical Pacific. *J. Atmos. Sci.*, **28**, 702–708, https://doi.org/10.1175/1520-0469(1971)028<0702:DOADOI>2.0.CO;2.

Manabe, S., and R. F. Strickler, 1964: Thermal equilibrium of the atmosphere with a convective adjustment. *J. Atmos. Sci.*, **21**, 361–385, https://doi.org/10.1175/1520-0469(1964)021<0361:TEOTAW>2.0.CO;2.

——, J. Smagorinsky, and R. F. Strickler, 1965: Simulated climatology of a general circulation model with a hydrologic cycle. *Mon. Wea. Rev.*, **93**, 769–798, https://doi.org/10.1175/1520-0493(1965)093<0769:SCOAGC>2.3.CO;2.

Mapes, B. E., 1997: Equilibrium vs. activation control of large-scale variations of tropical deep convection. *The Physics and Parameterization of Moist Atmospheric Convection*, Springer, 321–358, https://doi.org/10.1007/978-94-015-8828-7_13.

——, 2000: Convective inhibition, subgrid-scale triggering energy, and stratiform instability in a toy tropical wave model. *J. Atmos. Sci.*, **57**, 1515–1535, https://doi.org/10.1175/1520-0469(2000)057<1515:CISSTE>2.0.CO;2.

——, and R. Neale, 2011: Parameterizing convective organization to escape the entrainment dilemma. *J. Adv. Model. Earth Syst.*, **3**, M06004, https://doi.org/10.1029/2011MS000042.

——, A. S. Chandra, Z. Kuang, S. Song, and P. Zuidema, 2019: Estimating convection's moisture sensitivity: An observation–model synthesis using AMIE-DYNAMO field data. *J. Atmos. Sci.*, **76**, 1505–1520, https://doi.org/10.1175/JAS-D-18-0127.1.

Martinez-Villalobos, C., and J. D. Neelin, 2018: Shifts in precipitation accumulation extremes during the warm season over the United States. *Geophys. Res. Lett.*, **45**, 8586–8595, https://doi.org/10.1029/2018GL078465.

——, and ——, 2019: Why do precipitation intensities tend to follow gamma distributions? *J. Atmos. Sci.*, **76**, 3611–3631, https://doi.org/10.1175/JAS-D-18-0343.1.

Masunaga, H., 2012: A satellite study of the atmospheric forcing and response to moist convection over tropical and subtropical oceans. *J. Atmos. Sci.*, **69**, 150–167, https://doi.org/10.1175/JAS-D-11-016.1.

——, and B. E. Mapes, 2020: A mechanism for the maintenance of sharp tropical margins. *J. Atmos. Sci.*, **77**, 1181–1197, https://doi.org/10.1175/JAS-D-19-0154.1.

Mechem, D. B., R. A. Houze Jr., and S. S. Chen, 2002: Layer inflow into precipitating convection over the western tropical Pacific. *Quart. J. Roy. Meteor. Soc.*, **128**, 1997–2030, https://doi.org/10.1256/003590002320603502.

Moorthi, S., and M. J. Suarez, 1992: Relaxed Arakawa–Schubert: A parameterization of moist convection for general circulation models. *Mon. Wea. Rev.*, **120**, 978–1002, https://doi.org/10.1175/1520-0493(1992)120<0978:RASAPO>2.0.CO;2.

Neale, R. B., J. H. Richter, and M. Jochum, 2008: The impact of convection on ENSO: From a delayed oscillator to a series

of events. *J. Climate*, **21**, 5904–5924, https://doi.org/10.1175/2008JCLI2244.1.

Neelin, J. D., and J.-Y. Yu, 1994: Modes of tropical variability under convective adjustment and the Madden–Julian oscillation. Part I: Analytical theory. *J. Atmos. Sci.*, **51**, 1876–1894, https://doi.org/10.1175/1520-0469(1994)051<1876:MOTVUC>2.0.CO;2.

——, and N. Zeng, 2000: A quasi-equilibrium tropical circulation model—Formulation. *J. Atmos. Sci.*, **57**, 1741–1766, https://doi.org/10.1175/1520-0469(2000)057<1741:AQETCM>2.0.CO;2.

——, O. Peters, J. W.-B. Lin, K. Hales, and C. E. Holloway, 2008: Rethinking convective quasi-equilibrium: Observational constraints for stochastic convective schemes in climate models. *Philos. Trans. Roy. Soc. London*, **366A**, 2579–2602, https://doi.org/10.1098/rsta.2008.0056.

——, ——, and K. Hales, 2009: The transition to strong convection. *J. Atmos. Sci.*, **66**, 2367–2384, https://doi.org/10.1175/2009JAS2962.1.

——, S. Sahany, S. N. Stechmann, and D. N. Bernstein, 2017: Global warming precipitation accumulation increases above the current-climate cutoff scale. *Proc. Natl. Acad. Sci. USA*, **114**, 1258–1263, https://doi.org/10.1073/pnas.1615333114.

Peters, O., and J. D. Neelin, 2006: Critical phenomena in atmospheric precipitation. *Nat. Phys.*, **2**, 393–396, https://doi.org/10.1038/nphys314.

Plant, R., and G. C. Craig, 2008: A stochastic parameterization for deep convection based on equilibrium statistics. *J. Atmos. Sci.*, **65**, 87–105, https://doi.org/10.1175/2007JAS2263.1.

Powell, S. W., 2019: Observing possible thermodynamic controls on tropical marine rainfall in moist environments. *J. Atmos. Sci.*, **76**, 3737–3751, https://doi.org/10.1175/JAS-D-19-0144.1.

Qian, Y., and Coauthors, 2018: Parametric sensitivity and uncertainty quantification in the version 1 of E3SM atmosphere model based on short perturbed parameter ensemble simulations. *J. Geophys. Res. Atmos.*, **123**, 13 046–13 073, https://doi.org/10.1029/2018JD028927.

Raymond, D. J., 2001: A new model of the Madden–Julian oscillation. *J. Atmos. Sci.*, **58**, 2807–2819, https://doi.org/10.1175/1520-0469(2001)058<2807:ANMOTM>2.0.CO;2.

——, and X. Zeng, 2005: Modelling tropical atmospheric convection in the context of the weak temperature gradient approximation. *Quart. J. Roy. Meteor. Soc.*, **131**, 1301–1320, https://doi.org/10.1256/QJ.03.97.

——, and Ž. Fuchs, 2007: Convectively coupled gravity and moisture modes in a simple atmospheric model. *Tellus*, **59A**, 627–640, https://doi.org/10.1111/j.1600-0870.2007.00268.x.

——, and ——, 2009: Moisture modes and the Madden–Julian oscillation. *J. Climate*, **22**, 3031–3046, https://doi.org/10.1175/2008JCLI2739.1.

——, and M. J. Herman, 2011: Convective quasi-equilibrium reconsidered. *J. Adv. Model. Earth Syst.*, **3**, 2011MS000079, https://doi.org/10.1029/2011MS000079.

——, and M. M. Flores, 2016: Predicting convective rainfall over tropical oceans from environmental conditions. *J. Adv. Model. Earth Syst.*, **8**, 703–718, https://doi.org/10.1002/2015MS000595.

——, G. B. Raga, C. S. Bretherton, J. Molinari, C. López-Carrillo, and Ž. Fuchs, 2003: Convective forcing in the intertropical convergence zone of the eastern Pacific. *J. Atmos. Sci.*, **60**, 2064–2082, https://doi.org/10.1175/1520-0469(2003)060<2064:CFITIC>2.0.CO;2.

——, Ž. Fuchs, S. Gjorgjievska, and S. Sessions, 2015: Balanced dynamics and convection in the tropical troposphere. *J. Adv. Model. Earth Syst.*, **7**, 1093–1116, https://doi.org/10.1002/2015MS000467.

Rushley, S., D. Kim, C. Bretherton, and M.-S. Ahn, 2018: Reexamining the nonlinear moisture-precipitation relationship over the tropical oceans. *Geophys. Res. Lett.*, **45**, 1133–1140, https://doi.org/10.1002/2017GL076296.

Sahany, S., J. D. Neelin, K. Hales, and R. B. Neale, 2012: Temperature–moisture dependence of the deep convective transition as a constraint on entrainment in climate models. *J. Atmos. Sci.*, **69**, 1340–1358, https://doi.org/10.1175/JAS-D-11-0164.1.

Schiro, K. A., and J. D. Neelin, 2019: Deep convective organization, moisture vertical structure, and convective transition using deep-inflow mixing. *J. Atmos. Sci.*, **76**, 965–987, https://doi.org/10.1175/JAS-D-18-0122.1.

——, F. Ahmed, S. E. Giangrande, and J. D. Neelin, 2018: GoAmazon2014/5 campaign points to deep-inflow approach to deep convection across scales. *Proc. Natl. Acad. Sci. USA*, **115**, 4577–4582, https://doi.org/10.1073/pnas.1719842115.

Sessions, S. L., S. Sentić, and D. J. Raymond, 2019: Balanced dynamics and moisture quasi-equilibrium in DYNAMO convection. *J. Atmos. Sci.*, **76**, 2781–2799, https://doi.org/10.1175/JAS-D-18-0173.1.

Singh, M. S., and P. A. O'Gorman, 2013: Influence of entrainment on the thermal stratification in simulations of radiative-convective equilibrium. *Geophys. Res. Lett.*, **40**, 4398–4403, https://doi.org/10.1002/grl.50796.

Sobel, A. H., and C. S. Bretherton, 2000: Modeling tropical precipitation in a single column. *J. Climate*, **13**, 4378–4392, https://doi.org/10.1175/1520-0442(2000)013<4378:MTPIAS>2.0.CO;2.

——, and ——, 2003: Large-scale waves interacting with deep convection in idealized mesoscale model simulations. *Tellus*, **55A**, 45–60, https://doi.org/10.3402/tellusa.v55i1.12084.

——, and H. Gildor, 2003: A simple time-dependent model of SST hot spots. *J. Climate*, **16**, 3978–3992, https://doi.org/10.1175/1520-0442(2003)016<3978:ASTMOS>2.0.CO;2.

——, and E. Maloney, 2012: An idealized semi-empirical framework for modeling the Madden–Julian oscillation. *J. Atmos. Sci.*, **69**, 1691–1705, https://doi.org/10.1175/JAS-D-11-0118.1.

——, and ——, 2013: Moisture modes and the eastward propagation of the MJO. *J. Atmos. Sci.*, **70**, 187–192, https://doi.org/10.1175/JAS-D-12-0189.1.

——, J. Nilsson, and L. M. Polvani, 2001: The weak temperature gradient approximation and balanced tropical moisture waves. *J. Atmos. Sci.*, **58**, 3650–3665, https://doi.org/10.1175/1520-0469(2001)058<3650:TWTGAA>2.0.CO;2.

Stechmann, S. N., and J. D. Neelin, 2011: A stochastic model for the transition to strong convection. *J. Atmos. Sci.*, **68**, 2955–2970, https://doi.org/10.1175/JAS-D-11-028.1.

——, and ——, 2014: First-passage-time prototypes for precipitation statistics. *J. Atmos. Sci.*, **71**, 3269–3291, https://doi.org/10.1175/JAS-D-13-0268.1.

——, and S. Hottovy, 2017: Unified spectrum of tropical rainfall and waves in a simple stochastic model. *Geophys. Res. Lett.*, **44**, 10 713–10 724, https://doi.org/10.1002/2017GL075754.

Sugiyama, M., 2009: The moisture mode in the quasi-equilibrium tropical circulation model. Part I: Analysis based on the weak temperature gradient approximation. *J. Atmos. Sci.*, **66**, 1507–1523, https://doi.org/10.1175/2008JAS2690.1.

Sukhatme, J., 2014: Low-frequency modes in an equatorial shallow-water model with moisture gradients. *Quart. J. Roy. Meteor. Soc.*, **140**, 1838–1846, https://doi.org/10.1002/qj.2264.

Tian, Y., and Z. Kuang, 2019: Why does deep convection have different sensitivities to temperature perturbations in the lower versus upper troposphere? *J. Atmos. Sci.*, **76**, 27–41, https://doi.org/10.1175/JAS-D-18-0023.1.

Tulich, S. N., and B. E. Mapes, 2010: Transient environmental sensitivities of explicitly simulated tropical convection. *J. Atmos. Sci.*, **67**, 923–940, https://doi.org/10.1175/2009JAS3277.1.

Wang, S., and A. H. Sobel, 2011: Response of convection to relative sea surface temperature: Cloud-resolving simulations in two and three dimensions. *J. Geophys. Res.*, **116**, D11119, https://doi.org/10.1029/2010JD015347.

Wheeler, M., and G. N. Kiladis, 1999: Convectively coupled equatorial waves: Analysis of clouds and temperature in the wavenumber–frequency domain. *J. Atmos. Sci.*, **56**, 374–399, https://doi.org/10.1175/1520-0469(1999)056<0374:CCEWAO>2.0.CO;2.

Wolding, B., J. Dias, G. Kiladis, E. Maloney, and M. Branson, 2020: Interactions between moisture and tropical convection. Part II: The convective coupling of equatorial waves. *J. Atmos. Sci.*, **77**, 1801–1819, https://doi.org/10.1175/JAS-D-19-0226.1.

Yano, J.-I., and R. S. Plant, 2012: Convective quasi-equilibrium. *Rev. Geophys.*, **50**, RG4004, https://doi.org/10.1029/2011RG000378.

——, W. W. Grabowski, G. L. Roff, and B. E. Mapes, 2000: Asymptotic approaches to convective quasi-equilibrium. *Quart. J. Roy. Meteor. Soc.*, **126**, 1861–1887, https://doi.org/10.1002/qj.49712656615.

Yu, J.-Y., and J. D. Neelin, 1994: Modes of tropical variability under convective adjustment and the Madden–Julian oscillation. Part II: Numerical results. *J. Atmos. Sci.*, **51**, 1895–1914, https://doi.org/10.1175/1520-0469(1994)051<1895:MOTVUC>2.0.CO;2.

Zhang, C., 2005: Madden-Julian oscillation. *Rev. Geophys.*, **43**, RG2003, https://doi.org/10.1029/2004RG000158.

Zhang, G. J., 2009: Effects of entrainment on convective available potential energy and closure assumptions in convection parameterization. *J. Geophys. Res.*, **114**, D07109, https://doi.org/10.1029/2008JD010976.

——, and N. A. McFarlane, 1995: Sensitivity of climate simulations to the parameterization of cumulus convection in the Canadian Climate Centre general circulation model. *Atmos.–Ocean*, **33**, 407–446, https://doi.org/10.1080/07055900.1995.9649539.

Zhao, M., and Coauthors, 2018: The GFDL global atmosphere and land model AM4.0/LM4.0: 2. Model description, sensitivity studies, and tuning strategies. *J. Adv. Model. Earth Syst.*, **10**, 735–769, https://doi.org/10.1002/2017MS001209.